University of Strathclyde

Department of Naval Architecture, Ocean and Marine Engineering

PERIDYNAMICS AND ITS IMPLEMENTATION IN FINITE ELEMENT FRAMEWORK

By

Jeeyeon Heo

A thesis submitted in fulfilment of the requirements for the degree of

Master of Philosophy

Glasgow, U.K.

August 2019

DECLARATION

This thesis is the result of the author's original research. It has been composed by the author and has not been previously submitted for the examination which has led to the award of a degree.

Signed:

Date:

ACKNOWLEDGEMENTS

I want to express the deepest gratitude to my supervisor, Dr Erkan Oterkus, who guided me with passion, kindness, and encouragement for my M.Phill course.

I am very grateful to my family for their beliefs on my success.

Lastly, I would like to thank INHA University for financial support.

ABSTRACT

Predicting crack propagation and fracture is still a challenging research area. There are various methods for this, and the finite element method (FE method) is the most popular approach. The FE method is a powerful technology that can be used across multiple problems. However, because it is based on classical continuum mechanics (CCM), there are several disadvantages. Since the governing equation of CCM is a partial differential equation with a differential term for space, it is impossible to find the exact solution of the governing equation when spatial discontinuities exist which is caused by a crack. As an alternative approach Peridynamics is a method introduced to overcome the drawbacks of CCM. The governing equation of Peridynamics is form of an integral equation without spatial differentiation. Therefore, it is possible to analyse structures with cracks in which discontinuity in space exists.

Peridynamics is a mesh-free method in which each node interacts with other nodes in its vicinity. Because of this, researchers often use language-based programs that can easily calculate numerical values of parameters of interest. This feature make it difficult to attempt to apply peridynamics to various simulation fields. However, if a model is made by FE software based on peridynamic theory, it is possible to expand the simulation fields by utilizing functions of FE software.

In this thesis, various analyses are performed by implementing peridynamics in FE software. From the most basic isotropic material to an orthotropic plate, the simulations of the crack propagation were carried out. In addition, a peridynamic structure based on beam and plate theory were also modelled, and this model was compared with the results of the referenced papers. Furthermore, the buckling and free vibration analyses are performed for several cases to consider the effect of each parameter of the crack geometries on characteristics and stiffness of the plate.

CONTENTS

LIST OF TABLES

LIST OF FIGURES

NOMENCLATURE

A	Cross-sectional area of the beam
$\mathbf{b}$	Body force density field
$b_{(k)}$	Body force on material point (k)
c	Bond constant
c_b	Bending bond constant
c_f	Fibre bond constant
c_{in}	Interlayer normal bond constant
c_{is}	Interlayer shear bond constant
c_m	Matrix bond constant
c_s	Shear bond constant
δ	The horizon
Δx	Spacing between material points
E	Young's modulus
E_m	Young's modulus of matrix material
$E_{(k)(j)}$	Peridynamic Young's modulus of connection between material points (k) and (j)
$\boldsymbol{\eta}_{(k)(j)}$	Relative displacement vector between material points (k) and (j)
$\mathbf{F}^e_{(k)}$	External force acting on material point (k)
$\mathbf{F}^i_{(k)}$	Internal force acting on material point (k) caused by peridynamic interaction force

$\mathbf{f}$	Pairwise force density function
$\tilde{f}_{(k)(j)}$	Peridynamic bending force density between material points (k) and (j)
$\hat{f}_{(k)(j)}$	Peridynamic shear force density between material points (k) and (j)
G	Shear modulus
G_m	Shear modulus of matrix material
$G_{(k)(j)}$	Peridynamic shear modulus of connection between material points (k) and (j)
G_{IC}	Critical energy release rate of mode I
G_{IIC}	Critical energy release rate of mode II
$\bar{G}_{(k)(j)}$	Surface correction factor of the connection between material point (k) and (j)
$g_{(k)}$	Surface correction factor of material point (k)
h	Thickness of plate
$k_{(k)(j)}$	Peridynamic spring constant of connection between material points (k) and (j)
κ	Bulk modulus
$\kappa_{(k)(j)}$	Curvature between material point (k) and (j)
κ_{c}	Critical curvature
μ	History-dependent scalar-valued function
N	The number of material points within the horizon
φ	Local damage factor

$\varphi_{(k)(j)}$	Shear angle rotation between material point (k) and (j)
φ_c	Critical shear angel
$\phi_{(k)}$	Rotation of material point (k)
Q	The number of material points in fibre direction within the horizon
R_c	Fictitious material boundary layer
R_l	Loading material boundary layer
$\rho_{(k)}$	Mass density of the material point (k)
$s_{(k)(j)}$	Bond stretch between material points (k) and (j)
s_c	Critical bond stretch
$\boldsymbol{T}$	Total kinetic energy
θ	Fibre orientation
U	Total potential energy
$V_{(k)}$	Unit volume of material point (k)
W_{CM}	Strain energy density based on classical continuum mechanics
W_{PD}	Strain energy density based on Peridynamics
$w_{(k)}$	Transverse displacement of material point (k)
$\boldsymbol{\xi}_{(k)(j)}$	Relative position vector between material points (k) and (j)

1. INTRODUCTION

1.1 Overview

Fatigue and fracture caused by cracks are a prevalent problem in marine structures, and the damage is significant. Since the equation of motion of classical continuum mechanics (CCM) is based on the differential equations, it is not suitable for structures with discontinuities such as crack. There are several methods introduced to solve this problem, such as extended finite element method (XFEM), phase-field method (PFM), cohesive zone model (CZM) and Peridynamics. Above all, peridynamics was introduced by Silling [1] and the differential term of the equation of motion was reformulated as an integration term.

1.2 Motivation

Peridynamics was introduced to overcome the limitations of CCM. Therefore, it has the advantage of being able to analyse what cannot be done using CCM. Conversely, however, verification through comparisons with other method outcomes is essential because a different approach has been used. It is also possible to expand into a variety of fields by performing analyses on models containing discontinuities. By doing this, peridynamic model can use the analysis algorithms attached to FE software, such as modal and buckling analysis. In case of static analysis, the solution can be driven quicker than language-based program. In this thesis, the research an implementation of Peridynamics in FE framework was carried out.

1.3 Objectives

Peridynamics is suitable for analysis of cracking damage and fracture in ships and offshore platforms. It is possible to model a structure containing a crack and make various analyses. In this thesis, the main objective is the implementation of Peridynamics into a finite element framework and validation of its model. In particular, free vibration and buckling analyses were performed to show the change in characteristics of the plates containing crack. Besides, the influence of parameters on the properties of the plate was determined using various variables related to cracking.

2. LITERATURE REVIEWS

2.1 Free Vibration and Buckling of Cracked Plates

As the industry develops, various mechanical structures tend to become light and high-strength. The structures such as ships, offshore platforms and airplanes are severely damaged by buckling and have a significant impact on the stability of structures if cracks exist inside them. Therefore, reliability assessment is required for structures with defects to be used below the design load. Defects, such as cracks, not only change the vibration characteristics of a structure but are also critical factors that cause instability in the structure.

Krawczuk [2] studied the changes in eigenfrequencies of the supported and the cantilever plate according to the location of a crack. The influence of crack parameters was compared for not only the 1st mode but also the 6th mode. The eigenfrequency of plates affected by boundary conditions as well as the effect of the crack. Khedmati et al. [3] studied how the buckling load varies with the length, orientation and location of the crack. This paper shows that the change of plate characteristic is completely different depending on where the crack is located in centre or edge of a plate. Also, there are many types of research about buckling behaviour and free vibration analysis of a cracked plate. [4] [5]. Nerantzaki [6] used the analogue equation method (AEM) to get the buckling coefficient of plates with variable thickness. Also, there are studies about simulation of buckling and free vibration using the phase-field method. Minh [7] studied the cracked plate considering various factors and Doan [8] studied the cracked rectangular plate with variable thickness. Moreover, Zeng [9] studied side crack based on classical thin plate theory using the popular Ritz method. Kumar [10] used hierarchical trigonometric functions to estimate the buckling loads of cracked plates with various types of cracks and boundary conditions.

2.2 Implementation of Peridynamics in FE software

The implementation of peridynamic theory is generally done using language-based programmes such as FORTRAN, MATLAB and C++. Although this method is usually useful, it limits the expansion of the peridynamic theory because there are various available popular FE software packages. Peridynamics begin with changing the fundamental differential equation into an integral equation, not deviating from the existing dynamics. It means that the

peridynamic theory can be applied to FE software based on FE methods. Macek and Silling [11] presented how to implement peridynamics in ABAQUS, a commercial finite element software [12] and demonstrated this using several examples. Yang et al [13] also attempted to apply the peridynamic beam and plate theories into the FE framework. In this thesis, simulations of various cases were attempted based on this. Moreover, Madenci et al [14] developed the peridynamic model for deformation of orthotropic material.

3. PERIDYNAMIC THEORY

3.1 Basic Theory

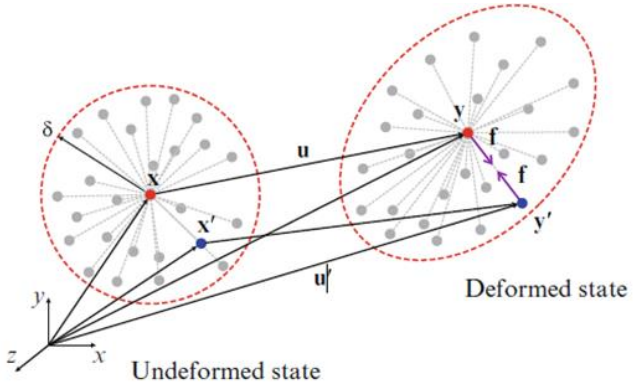

Figure 3.1 Undeformed and deformed state of peridynamic material points [15]

Peridynamic theory is one of the meshless methods introduced by S. Silling [1] to overcome the limitation of classical continuum mechanics (CCM). The most prominent feature of the peridynamic theory is that it replaces the spatial differential term of the equation of motion with an integral term. It assumes that the model consists of infinite nodes called material points. These points represent the unit volume of the model and interact with each other. As shown in Figure 3.1, it is assumed that when a model is deformed, the interaction force between the two points is equal and opposite, and this is called a bond-based peridynamics. In bond-based peridynamics, a material point only interacts with the material points within the horizon (δ). The material points that belong to the horizon is called family members. Due to these features, peridynamics has the advantage of being able to analyse various complex problems including a structure containing non-continuous geometry such as crack.

3.2 Equation of Motion

The peridynamic equation of motion can be derived from the principle of virtual work. The principle of virtual work is that when the system is at static equilibrium, the virtual work done by virtual displacement becomes zero. In the calculus of variation, the Lagrange's equation can be obtained, and it can derive the peridynamic equation of motion for material point (k).

$$\frac{d}{dt}\left(\frac{\partial L}{\partial \dot{\boldsymbol{q}}_{(k)}}\right) - \frac{\partial L}{\partial \boldsymbol{q}_{(k)}} = 0 \tag{3.1}$$

where Lagrangian (L) is defined as total kinetic energy (T) minus total potential energy (U). The total kinetic energy and total potential energy are calculated by summation of kinetic energy and potential energy of all material points. The substitution Lagrangian (L) in Eq. (3.1) for each material point results in the bond-based peridynamic equation of motion

$$\rho \ddot{\boldsymbol{u}} = \int_{H_x} \boldsymbol{f}(\boldsymbol{u}(\boldsymbol{x}', \boldsymbol{t}) - \boldsymbol{u}(\boldsymbol{x}, \boldsymbol{t}), \boldsymbol{x}' - \boldsymbol{x}) dV + \boldsymbol{b}(\boldsymbol{x}, t) \tag{3.2}$$

in which ρ is the mass density, H_{x} represent the neighbourhood region within the horizon of material point (**x**), **u** and **x** are displacement vector and position vector, respectively, and **b** represents the body force density exerting on the material point (**x**). Moreover, **f** is a force density vector of the pairwise interaction which can be expressed as

$$\boldsymbol{f}(\boldsymbol{u}' - \boldsymbol{u}, \boldsymbol{x}' - \boldsymbol{x}) = cs(\boldsymbol{u}' - \boldsymbol{u}, \boldsymbol{x}' - \boldsymbol{x}) \frac{\boldsymbol{y}' - \boldsymbol{y}}{|\boldsymbol{y}' - \boldsymbol{y}|} \tag{3.3a}$$

with

$$s(\boldsymbol{u}' - \boldsymbol{u}, \boldsymbol{x}' - \boldsymbol{x}) = \frac{|\boldsymbol{y}' - \boldsymbol{y}| - |\boldsymbol{x}' - \boldsymbol{x}|}{|\boldsymbol{x}' - \boldsymbol{x}|} = \frac{|\boldsymbol{\xi} + \boldsymbol{\eta}| - |\boldsymbol{\xi}|}{|\boldsymbol{\xi}|}, \tag{3.3b}$$

$$\boldsymbol{\xi} = \boldsymbol{x}' - \boldsymbol{x}, \tag{3.3c}$$

and

$$\boldsymbol{\eta} = \boldsymbol{u}' - \boldsymbol{u} \tag{3.3d}$$

where **y** is deformation vector that is summation of position vector (**x**) and displacement vector (**u**), $\boldsymbol{s}$ represents the stretch between material points, that is the ratio of distance change to the original distance between two material points, and $\boldsymbol{\xi}$ and $\boldsymbol{\eta}$ are relative position vector and relative displacement vector, respectively. The c parameter is a peridynamic parameter

called bond constant. It has a different value depending on the dimension of the model and is determined based on CCM that makes a material point has the same strain energy density with CCM [1]. The bond constant value of three-dimensional structure can be expressed as

$$c = \frac{18\kappa}{\pi\delta^4} \tag{3.4}$$

in which κ is bulk modulus and δ is the radius of the horizon. As expressed in Eq. (3.3a), the bond constant c is multiplied with stretch, and the value represents the force between the two points.

To solve the peridynamic equation of motion, the model should be discretised into finite number of material points. Based on Eq. (3.2). The equation of motion at material point (k) can be expressed in discretised form as

$$\rho_{(k)}\ddot{\boldsymbol{u}}_{(k)} = \sum_{j=1}^{N} \boldsymbol{f}\left(\boldsymbol{u}_{(j)} - \boldsymbol{u}_{(k)}, \boldsymbol{x}_{(j)} - \boldsymbol{x}_{(k)}\right)V_{(j)} + \boldsymbol{b}_{(k)} \tag{3.5}$$

where $\boldsymbol{\rho}_{(k)}$ is a mass density of material point (k), N is the number of the family members within the horizon, $\boldsymbol{u}_{(k)}$ is displacement at point (k), $V_{(j)}$ is a unit volume of family member point (j), and $\mathbf{b}_{(k)}$ is body force density at point (k).

When the bond stretch exceeds a particular value, called critical stretch, the bond disappears, that means removing of pairwise force between two material points. The critical stretch value is related to the energy release rate, which is required to break the bonds that are initially connected to separate the two halves of the body [1]. The critical stretch of elastic material can be expressed as

$$s_c = \sqrt{\frac{5G_{IC}}{9\kappa\delta}} \tag{3.6}$$

in which G_{IC} represents the energy release rate, κ is bulk modulus and δ is the radius of the horizon. In order to consider the crack propagation as a response to deformation, a history-dependent scalar-valued function is introduced as

$$\mu(\boldsymbol{x}_{(j)} - \boldsymbol{x}_{(k)}, t) = \begin{cases} 1 & if\ s_{(k)(j)}(t') < s_c \quad for\ all\ 0 < t' \\ 0 & otherwise \end{cases} \tag{3.7}$$

where s_c represents the critical stretch value and $s_{(k)(j)}$ represents the stretch value between two material points (k) and (j) calculated by (3.3a). The local damage at a material point is defined by the ratio of the number of broken bonds to initially connected bond. Moreover, each bond is weighted with unit volume.

$$\varphi = 1 - \frac{\int_H \mu(\boldsymbol{x}' - \boldsymbol{x}, t) dV'}{\int_H dV'} \tag{3.8}$$

This value ranges from 0 to 1. Zero means all bond connections are maintained and one means all connections are removed. When calculating the value from the plate having the initial crack, the value 0.3986 is obtained from the point near the crack. Therefore, it can be considered that the cracks have propagated when the value is greater than about 0.4.

3.3 Boundary conditions

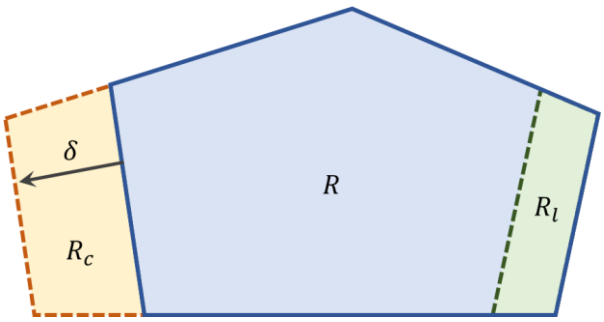

Figure 3.2 Application of boundary conditions in peridynamic theory

In peridynamic theory, the equation of motion does not contain spatial derivative terms. To apply boundary conditions, the model needs additional material points inside a fictitious material layer, R_c. This layer has a thickness equal to the radius of the horizon and boundary conditions such as displacement or rotation constraints can be applied. On the other hand, loading conditions like transverse load or moment, can be applied on a layer, R_l, within an actual solution domain. [15]

3.4 Surface Correction Factor

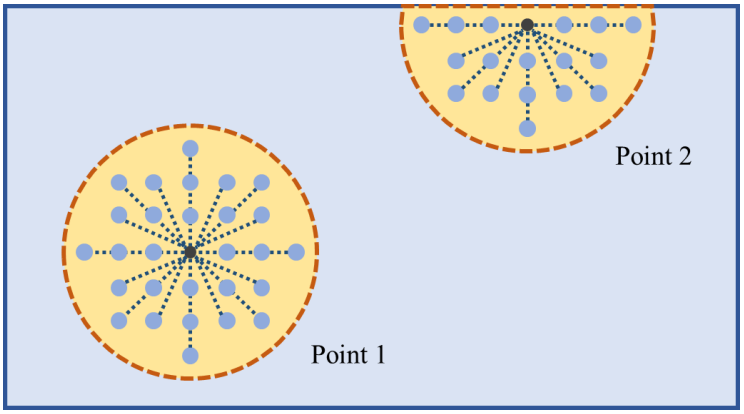

Figure 3.3 Peridynamic material points and horizon

The surface correction is required to get an accurate result in Peridynamics. The peridynamic theory is based on the relationships between the material points within the horizon. If the shape of the horizon is incomplete because a point is located near the surface of a model, as point 2 shown in Figure 3.3, that point cannot perform well as point 1. Because peridynamics satisfy all the conservation laws of the continuum mechanics, every material point should have the same strain energy at every location if uniform strain and stress conditions are satisfied. To satisfy these conditions, the surface correction factor are used in peridynamic theory. These correction factors are calculated as the ratio of peridynamic strain energy density to classical continuum mechanics strain energy density.

$$g_{(k)} = \frac{W^{CM}}{W^{PD}_{(k)}} \tag{3.9a}$$

$$\bar{g}_{(k)(j)} = \frac{g_{(k)} + g_{(j)}}{2} \tag{3.9b}$$

where W^{CM} and $W^{PD}_{(k)}$ represent strain energy at material point (k) based on classical continuum mechanics and peridynamics, respectively. Also, $g_{(k)}$ is the surface correction factor at material point (k). The peridynamic force exerts between two interacting material points. Thus, these surface correction factors are used by calculating the average value $\bar{g}_{(k)(j)}$ of two interacting material points (k) and (j). If the peridynamic model is two or three dimensional, the surface correction factor should be calculated for all directions, as x, y and z.

$$g_{\alpha(k)} = \frac{W_{\alpha}^{CM}}{W_{\alpha(k)}^{PD}} \tag{3.10a}$$

$$\bar{g}_{\alpha(k)(j)} = \frac{g_{\alpha(k)} + g_{\alpha(j)}}{2} \tag{3.10b}$$

$$\bar{G}_{(k)(j)} = \left[\left(\frac{n_x}{\bar{g}_{x(k)(j)}}\right)^2 + \left(\frac{n_y}{\bar{g}_{y(k)(j)}}\right)^2 + \left(\frac{n_z}{\bar{g}_{z(k)(j)}}\right)^2\right]^{-\frac{1}{2}} \tag{3.10c}$$

where $\bar{G}_{(k)(j)}$ represents surface correction factor of the bond between material points (k) and (j) with $(\alpha = x, y, z)$. And n_α corresponds to the unit relative position vector in α direction which is calculated as $n_\alpha = \left(\mathbf{x}_{\alpha(j)} - \mathbf{x}_{\alpha(k)}\right)/\left|\mathbf{x}_{(j)} - \mathbf{x}_{(k)}\right|$.

3.5 Implementation of Peridynamics in ANSYS

The peridynamic modelling is usually done by language-based programs such as MATLAB and FORTRAN. These methods are still useful in many cases. However, in some cases, it can be beneficial to use a commercial FE software to perform peridynamic simulations. In bond-based peridynamic theory, the material points only interact with the other points within their horizon. The interaction between two material points is called a bond and the interaction can be substituted by a spring for elastic interaction [11].

To convert the peridynamic parameters into FE parameters, the equation of motion of two approaches should be compared. This procedure can be derived using micro modulus tensor [16]. The unit of peridynamic equation of motion is based on force density, so the Eq. (3.5) should be multiplied with unit volume of material point (k).

$$\rho_{(k)}V_{(k)}\ddot{\boldsymbol{u}}_{(k)} = \sum_{j=1}^{N} c\frac{\left|\boldsymbol{\xi}_{(k)(j)} + \boldsymbol{\eta}_{(k)(j)}\right| - \xi_{(k)(j)}}{\xi_{(k)(j)}}V_{(j)}V_{(k)} + \boldsymbol{b}_{(k)}V_{(k)} \tag{3.11}$$

$$M_{(k)}\ddot{\boldsymbol{u}}_{(k)} = \boldsymbol{F}^{i}_{(k)} + \boldsymbol{F}^{e}_{(k)} \tag{3.12}$$

where $\rho_{(k)}V_{(k)}$ represent the mass of the material point (k), $M_{(k)}$. The force density vector $\mathbf{f}$ in Eq. (3.5) can be substituted by Eq. (3.3a). $\mathbf{F}^{i}_{(k)}$ represents the internal force caused by interaction force with family points, and $\mathbf{F}^{e}_{(k)}$ represents the external force that is acting on material point (k). If the bond interaction forces are considered as spring forces, a peridynamic spring constant can be obtained.

$$\boldsymbol{F}^{i}_{(k)} = \sum_{j=1}^{N} f_{(k)} \tag{3.13a}$$

$$f_{(k)} = c\frac{V_{(j)}V_{(k)}}{\xi_{(k)(j)}} \times \left(\left|\boldsymbol{\xi}_{(k)(j)} + \boldsymbol{\eta}_{(k)(j)}\right| - \xi_{(k)(j)}\right) \tag{3.13b}$$

where the first term on the right side of Eq. (3.13a) can be expressed as a summation of spring forces. According to Hooke's law, the spring force equals to a spring constant k times change

in length. Therefore, the peridynamic spring constnat of the bond between material points (k) and (j) is described as

$$k_{(k)(j)} = \frac{c}{\xi_{(k)(j)}} V_{(j)} V_{(k)} \tag{3.14}$$

where $\xi_{(k)(j)}$ represents the length of the interaction bond. This peridynamic spring constant should be multiplied with surface correction factor and volume correction factor of each bond.

ANSYS, a commercial finite element software, is used for peridynamic simulations. It has various element types to analyse. The two-dimensional plate can be modelled using COMBIN14 element. It is a uniaxial tension-compression element with three degrees of freedom at each node. The bending and torsion are not considered, and the only information that this element needs is spring constant given in Eq. (3.14). This element has no mass. Therefore to solve the time-dependent dynamic problems, the mass should be added using mass element, MASS21. When generating a peridynamic model, firstly nodes are created equally spaced as material points. Subsequently, each node is connected with the family nodes by COMBIN14 element. Each element has different spring constant because of correction factors. As shown in Figure 3.4, every node interacts with other nodes through a network of web.

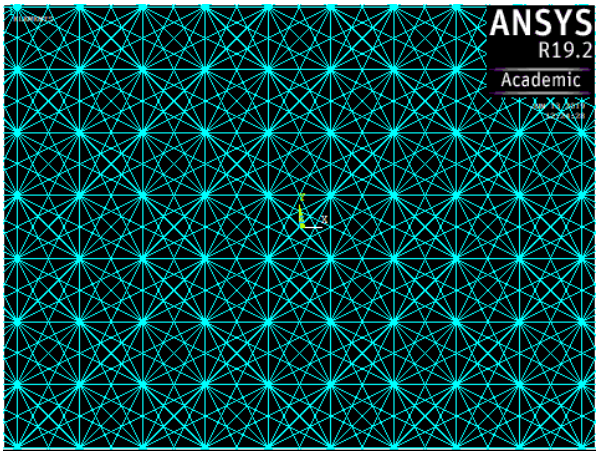

Figure 3.4 Peridynamic connections of material points with family members

4. PERIDYNAMIC BEAM AND PLATE FORMULATION

The classical peridynamic theory is only considers translational degrees of freedom (DOF). To derive the kinematic equations of beams and plates requires to take into account out-of-plane deformation and rotations [17]. The approach is similar to the original peridynamic theory. Every material point has each transverse displacement and rotation as DOF and interacts with other material points located inside their horizon. In this chapter, the process of deriving the equation of motion of Timoshenko beam and Mindlin plate is described.

4.1 Timoshenko Beam Equation of Motion

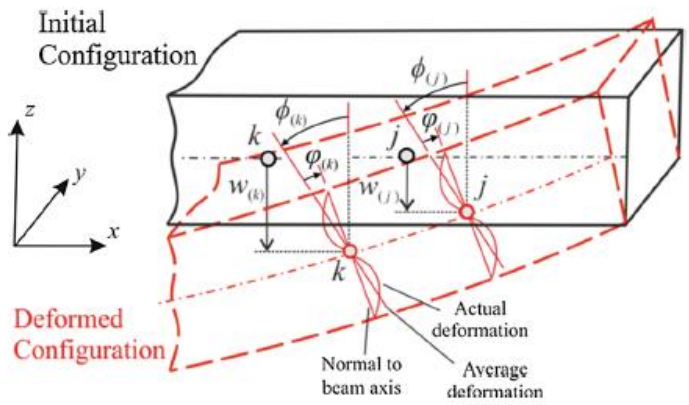

Figure 4.1 Initial and deformed configurations of peridynamic Timoshenko beam [17]

There are two different peridynamic interaction force densities between material points; transverse shear force and bending moment, respectively,

$$\hat{f}_{(k)(j)} = c_s \varphi_{(k)(j)} \tag{4.1a}$$

$$\tilde{f}_{(k)(j)} = c_b \kappa_{(k)(j)} \tag{4.1b}$$

in which c_s and c_b are peridynamic parameters called bond constants that are related with shear angle $\varphi_{(k)(j)}$ and curvature $\kappa_{(k)(j)}$, respectively, between material points (k) and (j). The shear angle and curvature arising from the interaction between material points can be described as

$$\varphi_{(k)(j)} = \left(\frac{w_{(j)} - w_{(k)}}{\xi_{(j)(k)}} - \frac{\phi_{(j)} + \phi_{(k)}}{2} sgn\left(x_{(j)} - x_{(k)}\right) \right) \tag{4.2a}$$

$$\kappa_{(k)(j)} = \frac{\phi_{(j)} - \phi_{(k)}}{\xi_{(j)(k)}} \tag{4.2b}$$

As referred above, the peridynamic equation of motion of the Timoshenko beam can be derived from Lagrange's equation given in Eq. (3.1). The peridynamic total kinetic energy is summation of kinetic energy caused by vertical translation and rotation, and peridynamic total potential energy is summation of strain every caused by shear distortion and bending of all material points. The total kinetic energy (T) and total potential energy (U) of the Timoshenko beam can be expressed as

$$T = \frac{1}{2} \sum_{k=1}^{\infty} \rho \left[\left(\dot{w}_{(k)} \right)^2 + \frac{I}{A} \left(\dot{\phi}_{(k)} \right)^2 \right] V_{(k)} \tag{4.3a}$$

and

$$\begin{aligned} U = & \sum_{k=1}^{\infty} \frac{1}{2} \left\{ \sum_{j=1}^{\infty} \frac{1}{2} \left[\widehat{w}_{(k)(j)} \left(\varphi_{(k)(j)} \right) + \widehat{w}_{(j)(k)} \left(\varphi_{(j)(k)} \right) \right] V_{(j)} - \hat{b}_{(k)} w_{(k)} \right\} V_{(k)} \\ & + \sum_{k=1}^{\infty} \frac{1}{2} \left\{ \sum_{j=1}^{\infty} \frac{1}{2} \left[\widetilde{w}_{(k)(j)} \left(\kappa_{(k)(j)} \right) + \widetilde{w}_{(j)(k)} \left(\kappa_{(j)(k)} \right) \right] V_{(j)} - \tilde{b}_{(k)} \phi_{(k)} \right\} V_{(k)} \end{aligned} \tag{4.3b}$$

in which ρ, I and A are mass density, moment of inertia and cross-sectional area, respectively. $\widehat{w}_{(k)(j)}$ and $\widetilde{w}_{(k)(j)}$ are micro-potentials, that is strain energy density of material point (k) caused by family point (j) arising from shear deformation and bending. Substituting Eqs. (4.3a) into (3.1), and replacing $\mathbf{q}_{(k)}$ with $w_{(k)}$ or $\phi_{(k)}$, result in two-equations of motion

$$\rho \ddot{w}_{(k)} = \sum_{j=1}^{\infty} c_s \left(\frac{w_{(j)} - w_{(k)}}{\xi_{(j)(k)}} - \frac{\phi_{(j)} + \phi_{(k)}}{2} sgn\left(x_{(j)} - x_{(k)}\right) \right) V_{(j)} + \hat{b}_{(k)} \tag{4.4a}$$

and

$$\rho \frac{I}{A} \ddot{\phi}_{(k)} = \sum_{j=1}^{\infty} c_b \left(\frac{\phi_{(j)} - \phi_{(k)}}{\xi_{(j)(k)}} \right) V_{(j)} + \frac{1}{2} \sum_{j=1}^{\infty} c_s \left(\frac{w_{(j)} - w_{(k)}}{\xi_{(j)(k)}} sgn\left(x_{(j)} - x_{(k)}\right) - \frac{\phi_{(j)} + \phi_{(k)}}{2} \right) \xi_{(j)(k)} V_{(j)} + \tilde{b}_{(k)} \quad (4.4b)$$

In the case of Timoshenko beam, the peridynamic bond constant values, c_s and c_b, can be defined as [17]

$$c_s = \frac{2k_s G}{A\delta^2} \quad (4.5a)$$

$$c_b = \frac{2EI}{A^2\delta^2} \quad (4.5b)$$

where E, G are Young's modulus and shear modulus, respectively, and A, I and k_s are cross-sectional area, moment of inertia and shear correction factor of the beam. When the cross-sectional area is rectangular, the shear correction factor, k_s, is equal to $5/6$ [18].

4.2 Mindlin Plate Equation of Motion

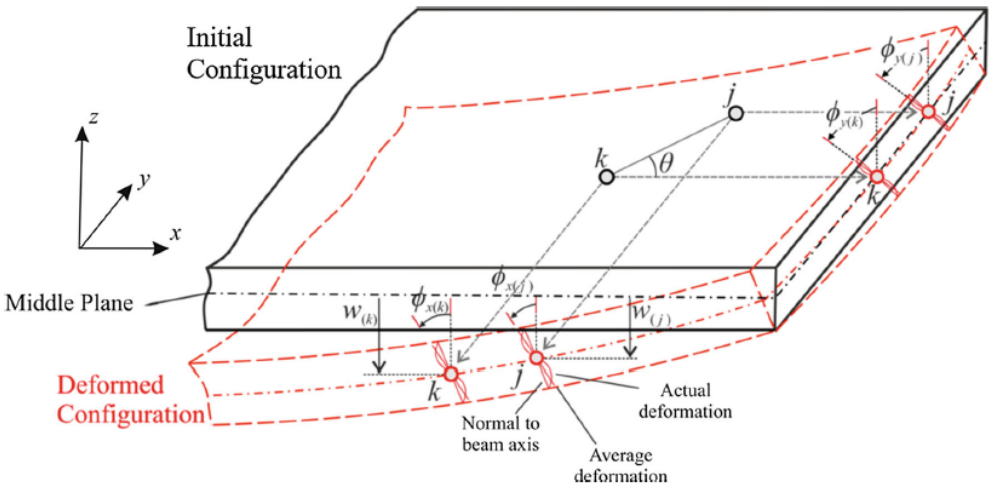

Figure 4.2 Initial and deformed configurations of peridynamic Mindlin plate [17]

The equation of motion of the Mindlin plate can be derived by the same procedure used for the Timoshenko beam. However, in the case of the plate, the shear angle is separated into x- and y-directions

$$\begin{aligned}\phi_{(k)} &= \phi_{x(k)}\cos\theta + \phi_{y(k)}\sin\theta \\ \phi_{(j)} &= \phi_{x(j)}\cos\theta + \phi_{y(j)}\sin\theta\end{aligned} \tag{4.6}$$

where θ is the orientation of the bond between material points (k) and (j). The total kinetic energy and total potential energy of the Mindlin plate is given as

$$T = \frac{1}{2}h\rho\sum_{k=1}^{\infty}\left[\frac{h^2}{12}\dot{\phi}^2{}_{x(k)} + \frac{h^2}{12}\dot{\phi}^2{}_{y(k)} + \dot{w}^2{}_{(k)}\right]A_{(k)} \tag{4.7a}$$

and

$$\begin{aligned}U = &\sum_{k=1}^{\infty}\frac{1}{2}\left\{\sum_{j=1}^{\infty}\frac{1}{2}\left[\hat{w}_{(k)(j)}\left(\varphi_{(k)(j)}\right) + \hat{w}_{(j)(k)}\left(\varphi_{(j)(k)}\right)\right]V_{(j)} - \hat{b}_{(k)}w_{(k)}\right\}V_{(k)} \\ &+ \sum_{k=1}^{\infty}\frac{1}{2}\left\{\sum_{j=1}^{\infty}\frac{1}{2}\left[\tilde{w}_{(k)(j)}\left(\kappa_{(k)(j)}\right) + \tilde{w}_{(j)(k)}\left(\kappa_{(j)(k)}\right)\right]V_{(j)} - \tilde{b}_{\alpha(k)}\phi_{\alpha(k)}\right\}V_{(k)}\end{aligned} \tag{4.7b}$$

in which h is the thickness of the plate, $A_{(k)}$ is the cross-sectional area of the material point (k), and α can be x or y. The three equations of motion can be obtained by substituting Eqs. (4.7a) into (3.1) and replacing $\mathbf{q}_{(k)}$ with $w_{(k)}$, $\phi_{x(k)}$ and $\phi_{y(k)}$ as

$$\rho h\ddot{w}_{(k)} = \sum_{j}^{\infty} c_s \left(\frac{w_{(j)} - w_{(k)}}{\xi_{(j)(k)}} - \frac{\phi_{x(j)} + \phi_{x(k)}}{2} cos\,\theta - \frac{\phi_{y(j)} + \phi_{y(k)}}{2} sin\,\theta \right) V_{(j)} + \hat{b}_{(k)} h, \tag{4.8a}$$

$$\frac{\rho h^3}{12} \ddot{\phi}_{x(k)} = c_b \sum_{j}^{\infty} \left(\frac{\phi_{x(j)} - \phi_{x(k)}}{\xi_{(j)(k)}} cos\,\theta + \frac{\phi_{y(j)} - \phi_{y(k)}}{\xi_{(j)(k)}} sin\,\theta \right) cos\,\theta\, V_{(j)} + \frac{1}{2} c_s \sum_{j}^{\infty} \xi_{(j)(k)} \left(\frac{w_{(j)} - w_{(k)}}{\xi_{(j)(k)}} - \frac{\phi_{x(j)} + \phi_{x(k)}}{2} cos\,\theta - \frac{\phi_{y(j)} + \phi_{y(k)}}{2} sin\,\theta \right) cos\,\theta\, V_{(j)} + \tilde{b}_{x(k)} h \tag{4.8b}$$

and

$$\frac{\rho h^3}{12} \ddot{\phi}_{y(k)} = c_b \sum_{j}^{\infty} \left(\frac{\phi_{x(j)} - \phi_{x(k)}}{\xi_{(j)(k)}} cos\,\theta + \frac{\phi_{y(j)} - \phi_{y(k)}}{\xi_{(j)(k)}} sin\,\theta \right) sin\,\theta\, V_{(j)} + \frac{1}{2} c_s \sum_{j}^{\infty} \xi_{(j)(k)} \left(\frac{w_{(j)} - w_{(k)}}{\xi_{(j)(k)}} - \frac{\phi_{x(j)} + \phi_{x(k)}}{2} cos\,\theta - \frac{\phi_{y(j)} + \phi_{y(k)}}{2} sin\,\theta \right) sin\,\theta\, V_{(j)} + \tilde{b}_{y(k)} h \tag{4.8c}$$

Peridynamic parameters c_s and c_b can be expressed as

$$c_s = \frac{9E}{4\pi\delta^3} k_s^2 \; and \; c_b = \frac{3h^2 E}{4\pi\delta^3} \tag{4.9}$$

where k_s represent the shear correction factor, and the value $\pi^2/12$ is used in most of plate [18].

Because the beam and plate peridynamic formulations use different displacement factor, $\kappa_{(k)(j)}$ and $\varphi_{(k)(j)}$, it needs different critical factor that determines the failure timing. The critical curvature and shear angle to define the failure of bonds can be expressed as [17]

$$\kappa_c = \sqrt{\frac{4G_{Ic}}{c_b h \delta^4}} \text{ and } \varphi_c = \sqrt{\frac{4G_{IIIc}}{c_s h \delta^4}} \tag{4.10}$$

where G_{Ic} and G_{IIIc} are Mode-I and Mode-III failure energy release rate, respectively.

4.3 Implementation of Timoshenko Beam and Mindlin Plate in ANSYS

To analyze the Timoshenko beam and Mindlin plate using ANSYS, a different element type is needed rather than using COMBIN14, because this element type can only consider translational DOF. However, the beam and plate formulations require rotational DOFs. The element type BEAM4 is suitable for these type of formulations. It is a uniaxial element with tension, compression, torsion, and bending capabilities. It has six degrees of freedom at each node, not only translations but also rotations. The peridynamic parameters can be converted through a similar procedure as in chapter 3.5. The Eqs. (4.4a) can be rewritten by multiplying with unit volume of point (k) as

$$\rho V_{(k)}\ddot{w}_{(k)} = \sum_{j=1}^{\infty} c_s \varphi_{(k)(j)} V_{(j)} V_{(k)} + \hat{b}_{(k)} V_{(k)} \tag{4.11a}$$

and

$$\rho V_{(k)} \frac{I}{A} \ddot{\phi}_{(k)} = \sum_{j=1}^{\infty} c_b \kappa_{(k)(j)} V_{(j)} V_{(k)} + \frac{1}{2} \sum_{j=1}^{\infty} c_s \varphi_{(k)(j)} \xi_{(j)(k)} V_{(j)} V_{(k)} + \tilde{b}_{(k)} V_{(k)} \tag{4.11b}$$

where $\rho V_{(k)}$ is the mass of the material point, c_s and c_b represent the shear bond constant and bending bond constant, respectively. The shear force and bending moment arising from the interactions can be described as

$$\hat{f}_{(k)} = c_s V_{(j)} V_{(k)} \varphi_{(k)(j)} \tag{4.12a}$$

$$\tilde{f}_{(k)} = c_b V_{(j)} V_{(k)} \kappa_{(k)(j)} \tag{4.12b}$$

According to classical continuum mechanics, the shear force and bending moment of Timoshenko beam can be described as

$$\hat{f}_{(k)(j)} = k_s A G_{(k)(j)} \varphi_{(k)(j)} \tag{4.13a}$$

$$\tilde{f}_{(k)(j)} = E_{(k)(j)} I_y \kappa_{(k)(j)} \tag{4.13b}$$

where $G_{(k)(j)}$ and $E_{(k)(j)}$ represent peridynamic shear modulus and Young's modulus of the bond between material points (k) and (j). k_s, A and I_y represent shear correction factor, cross-sectional area and moment of inertia of beam, respectively. These three parameters, i.e. k_s, A and I_y, are geometrical properties that are calculated based on the space between material points and plate thickness. Therefore, these values cannot be changed $G_{(k)(j)}$ and $E_{(k)(j)}$ can be converted into peridynamic parameters. Using Eqs. (4.12a) and Eqs. (4.13a), the peridynamic shear modulus and Young's modulus of Timoshenko beam can be expressed as

$$G_{(k)(j)} = \frac{c_s}{k_s A} V_{(j)} V_{(k)} \tag{4.14a}$$

and

$$E_{(k)(j)} = \frac{c_b}{I_y} V_{(j)} V_{(k)} \tag{4.14b}$$

in which these material parameters do not represent actual material parameters. Instead, they are calibration parameters for peridynamic simulations.

The peridynamic material parameters of the Mindlin plate for FEM can be obtained using the same process based on the equation of motion (EOM) of Mindlin plate, Eqs. (4.8a). The only difference is the unit of the equation of motion. The unit of EOM of Timoshenko beam, Eqs. (4.4a), is N/m^3 that of the force density, while unit of EOM of Mindlin plate, Eqs. (4.8a), is N/m^3·m that of the force density times length. Therefore, every term in Eqs. (4.8a) should be multiplied with unit volume $V_{(k)}$ and divided by plate thickness h,

$$\rho V_{(k)} \ddot{w}_{(k)} = \sum_{j=1}^{\infty} \frac{c_s}{h} \varphi_{(k)(j)} V_{(j)} V_{(k)} + \hat{b}_{(k)} V_{(k)}, \tag{4.15a}$$

$$\rho V_{(k)} \frac{I}{A} \ddot{\phi}_{x(k)} = \sum_{j=1}^{\infty} \frac{c_b}{h} \kappa_{(k)(j)} V_{(j)} V_{(k)} + \frac{1}{2} \sum_{j=1}^{\infty} \frac{c_s}{h} \varphi_{(k)(j)} \xi_{(j)(k)} \cos\theta \, V_{(j)} V_{(k)} + \tilde{b}_{x(k)} V_{(k)}, \tag{4.15b}$$

and

$$\rho V_{(k)} \frac{I}{A} \ddot{\phi}_{y(k)} = \sum_{j=1}^{\infty} \frac{c_b}{h} \kappa_{(k)(j)} V_{(j)} V_{(k)} + \frac{1}{2} \sum_{j=1}^{\infty} \frac{c_s}{h} \varphi_{(k)(j)} \xi_{(j)(k)} \sin\theta \, V_{(j)} V_{(k)} + \tilde{b}_{y(k)} V_{(k)} \tag{4.15c}$$

Peridynamic bond forces can be expressed same way with Eqs. (4.12a) as

$$\hat{f}_{(k)} = \frac{c_s}{h} V_{(j)} V_{(k)} \varphi_{(k)(j)} \tag{4.16a}$$

$$\tilde{f}_{(k)} = \frac{c_b}{h} V_{(j)} V_{(k)} \kappa_{(k)(j)} \tag{4.16b}$$

Therefore, the peridynamic material parameters of the Mindlin plate for FEM are described as

$$G_{(k)(j)} = \frac{c_s}{k_s A h} V_{(j)} V_{(k)} \tag{4.17a}$$

$$E_{(k)(j)} = \frac{c_b}{I_y h} V_{(j)} V_{(k)} \tag{4.17b}$$

As mentioned above, these coefficients are calibration parameters for peridynamic simulation.

5. PERIDYNAMICS FOR LAMINATED COMPOSITE MATERIAL

Composite material is a combination of two or more materials to make improvement in properties compared to individual components used alone. The primary purposes of these combinations are high strength. Composite material consists of a reinforcement and a matrix phase. The matrix phase has low strength and stiffness but high ductility, and it plays a role that keeps reinforcements together. The reinforcements function is to provide strength and stiffness. There are different types of composite materials. This chapter describes the unidirectional fibre-reinforced composite material.

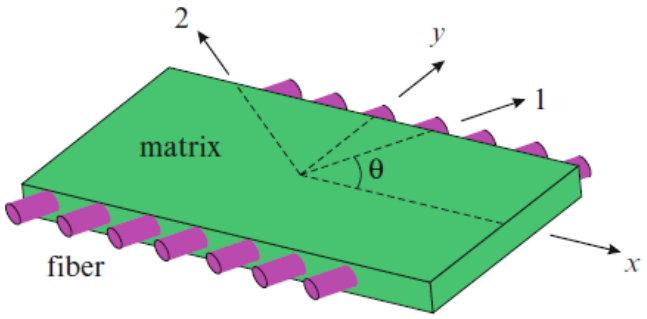

Figure 5.1 Natural and reference coordinate systems for fibre-reinforced lamina [15]

The fibre-reinforced material has extreme strength and stiffness in the fibre direction but very weak in the perpendicular direction to the fibre. In Figure 5.1, θ is the fibre orientation angle. One layer (ply) of a composite material is called a lamina. When multiple plies are stacked together, it is called laminate.

5.1 Laminated Composite

A lamina can be idealized into a two-dimensional plate. Each ply is discretized single layer of material points in the direction of its thickness. As shown in Figure 5.2, the material point i interacts with family points within its horizon. Fibre reinforced lamina has different peridynamic parameters according to the bond direction. The interaction bond in fibre direction and other directions are called fibre bond and matrix bond, respectively.

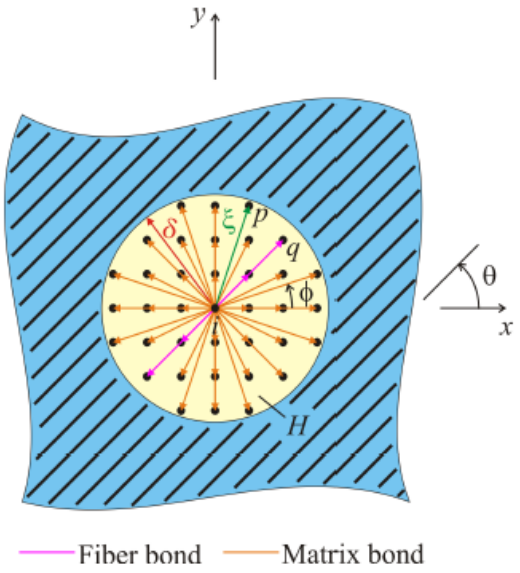

Figure 5.2 PD horizon for a lamina with a fibre orientation of *θ,* fibre and matrix bonds [19]

$$c = \begin{cases} c_f + c_m & for \phi = \theta \\ c_m & for \phi \neq \theta \end{cases} \tag{5.1}$$

in which θ is the fibre orientation and ϕ is the bond angle of each bond interaction. c_f and c_m are fibre bond constant and matrix bond constant, respectively. If the plate is isotropic material, the fibre bond constant c_f becomes zero and only the matrix bond constant c_m exists. Bond constants can be described as

$$c_f = \frac{2(Q_{11} - Q_{22})}{\sum_{q=1}^{Q} \xi_{qi} V_q} \tag{5.2a}$$

$$c_m = \frac{24 Q_{12}}{\pi h \delta^3} \tag{5.2b}$$

where V_q is the unit volume of the material points in the fibre direction, and ξ_{qi} is the distance from the reference point to family material points, especially along the fibre direction. Q represents the number of material points in the fibre direction, and h represents the thickness of each ply. $Q_{\alpha\alpha}$ is the components of stiffness matrix $\mathbf{Q}$ related to stress and strain,

$$\begin{Bmatrix}\sigma_{11}\\ \sigma_{22}\\ \sigma_{12}\end{Bmatrix}=\begin{bmatrix}Q_{11} & Q_{12} & 0\\ Q_{12} & Q_{22} & 0\\ 0 & 0 & Q_{66}\end{bmatrix}\begin{Bmatrix}\varepsilon_{11}\\ \varepsilon_{22}\\ \gamma_{12}\end{Bmatrix} \tag{5.3}$$

where

$$Q_{11}=\frac{E_1}{1-\nu_{21}\nu_{12}}$$

$$Q_{12}=\frac{\nu_{12}E_2}{1-\nu_{21}\nu_{12}} \tag{5.4}$$

$$Q_{22}=\frac{E_2}{1-\nu_{21}\nu_{12}}$$

$$Q_{66}=G_{12}$$

The strain energy density of material point (k) in single layer lamina for a uniaxial strain condition can be expressed by summation of the strain energy density of fibre bond and matrix bond as

$$W=W_f+W_m \tag{5.5a}$$

$$W_{CM}=\frac{1}{2}(Q_{11}-Q_{22})\zeta^2+\frac{1}{2}Q_{22}\zeta^2 \tag{5.5b}$$

$$W_{PD}=\frac{1}{2}\sum_{q=1}^{Q}\frac{1}{2}c_f s_{(i)(q)}^2\xi_{(i)(q)}V_{(q)}+\frac{1}{2}\sum_{j=1}^{N}\frac{1}{2}c_m s_{(i)(j)}^2\xi_{(i)(j)}V_{(j)} \tag{5.5c}$$

where W_f and W_m are strain energy densities arising from fibre bond and matrix bond. W_{CM} and W_{PD} represent the strain energy density of a single material point based on classical continuum mechanics and peridynamics, respectively. The $s_{(i)(j)}$ and $\xi_{(i)(j)}$ are the stretch and distance between material points (i) and (j), respectively.

5.2 Implementation of Peridynamic Formulation for a Lamina Plate in ANSYS

The peridynamic implementation in ANSYS for composites is similar to the basic application described in chapter 3.5. Each bond is represented with a spring element. In this thesis, the application of ANSYS is performed only for a composite lamina. The equation of motion can be expressed as

$$\rho_{(k)}V_{(k)}\ddot{\boldsymbol{u}}_{(k)} = \sum_{j=1}^{N}\left(c_m + \alpha c_f\right)\frac{\left|\boldsymbol{\xi}_{(k)(j)} + \boldsymbol{\eta}_{(k)(j)}\right| - \xi_{(k)(j)}}{\xi_{(k)(j)}}V_{(j)}V_{(k)} + \boldsymbol{b}_{(k)}V_{(k)} \tag{5.6}$$

In which $\rho_{(k)}V_{(k)}$ represent the mass of material point k. The c_m and c_f are peridynamic bond constants of matrix bond and fibre bond, respectively. α is value that depending on bond type.

$$\alpha = \begin{cases} 1 & for\, \phi = \theta \\ 0 & for\, \phi \neq \theta \end{cases} \tag{5.7}$$

This means if the bond angle and fibre orientation match, the material has a stronger connection than the other directions. The procedure to calculate the peridynamic spring constant is the same as described in chapter 3.5. The peridynamic spring constant of connection between material points k and j for a lamina can be expressed as

$$k_{(k)(j)} = \frac{c_m + \alpha c_f}{\xi_{(k)(j)}}V_{(j)}V_{(k)} \tag{5.8}$$

5.2.1 Numerical Results

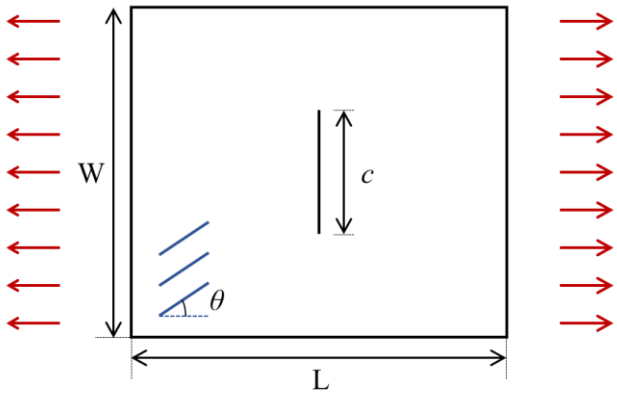

Figure 5.3 The geometry of the unidirectional lamina with a crack under tension loading

The fibre-reinforced lamina with a fibre orientation of 0°, 45° and 90° are considered as shown in Figure 5.3. The length and width of the plate are specified as $\mathrm{L} = 152.4$mm and $\mathrm{W} = 76.2$mm. It has a thickness of $\mathrm{h} = 0.1651$mm. Young's modulus in fibre and transverse directions are $E_{11} = 159.96$ GPa and $E_{22} = 8.96$ GPa, respectively. The shear modulus and Poisson's ratio are $G_{12} = 3.0054$ GPa and $1/3$. The material properties of matrix element which determine the peridynamic bond constants are $E_m = 3.7919$ GPa and $G_m = 1.4220$ GPa. The plate has a vertical crack at the centre, and its length is 17.78mm. The plate is subjected to velocity boundary conditions of $v_0 = 2.02 \times 10^{-7}$m/s in opposite directions along each edge. [19]

The results calculated by MATLAB and ANSYS are shown in Figure 5.4 and Figure 5.5, respectively. 28,800 material points are used in MATLAB and 20,000 points in ANSYS to reduce the computational time. The crack propagated along the fibre direction, and this is because the bond in the transverse direction is weaker than others. Thus, the bond perpendicular to hardening direction is broken first, which means that the force in that direction is lost. Continuously, the two points which belong to broken bond gradually move away from each other, and the crack progresses in the direction of the fibre.

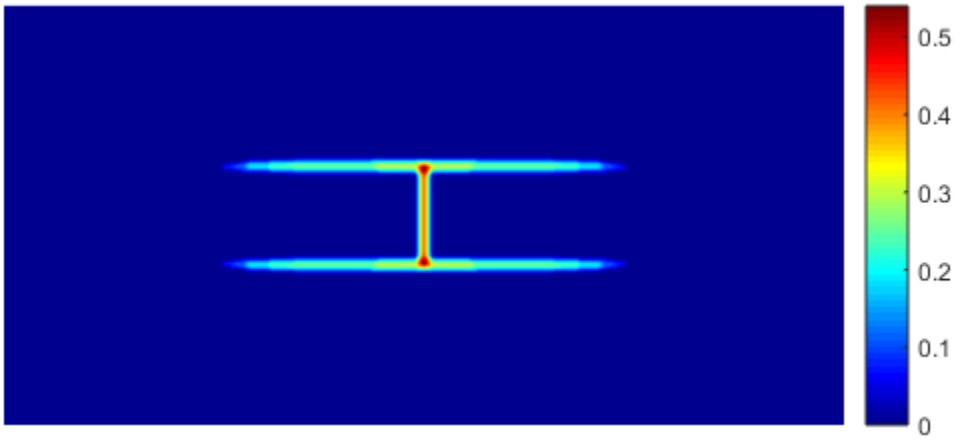

(a)

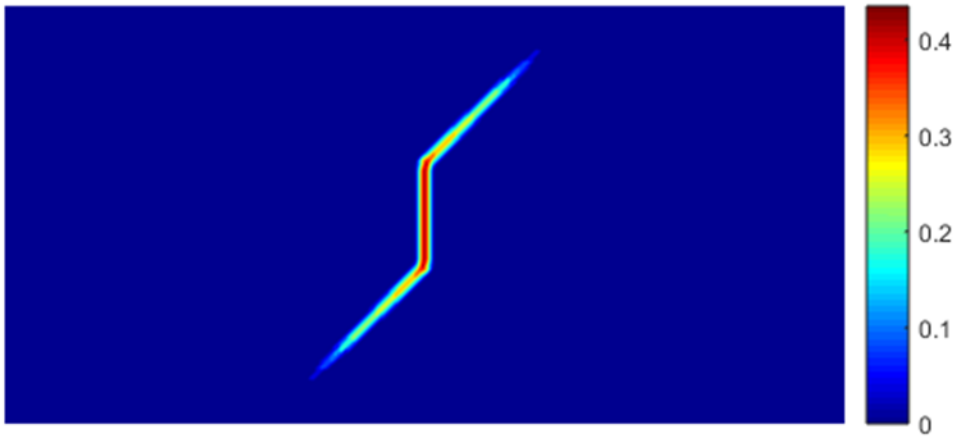

(b)

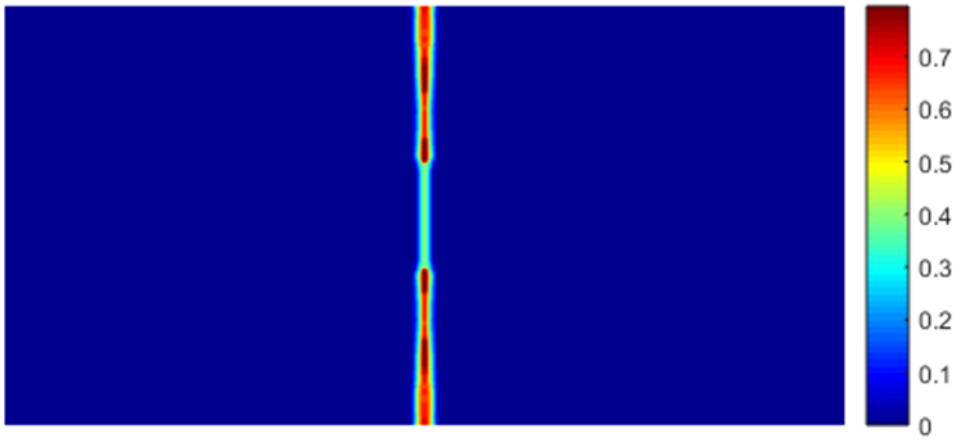

(c)

Figure 5.4 MATLAB results for the damage the plot of cracked lamina plate with fibre orientation of (a) $\theta = 0°$, (b) $\theta = 45°$ and (c) $\theta = 90°$

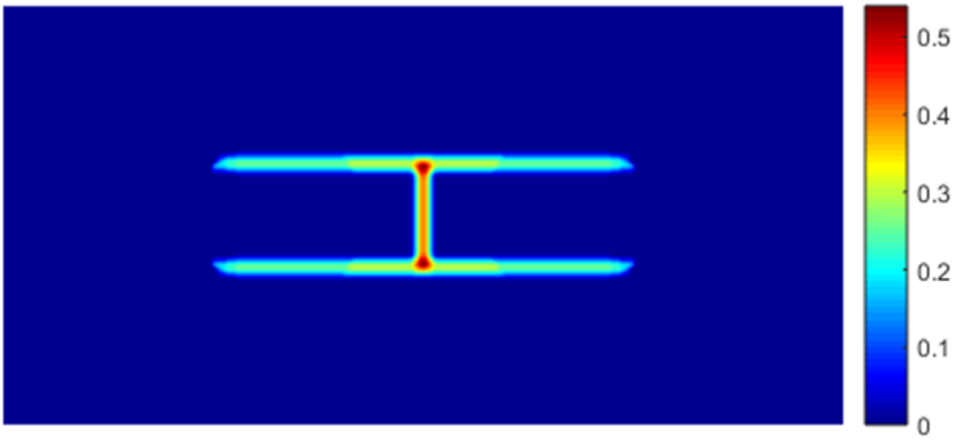

(a)

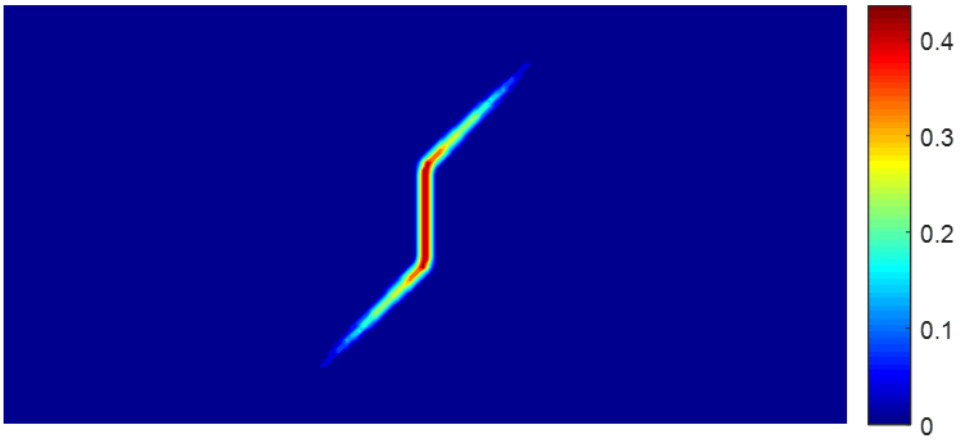

(b)

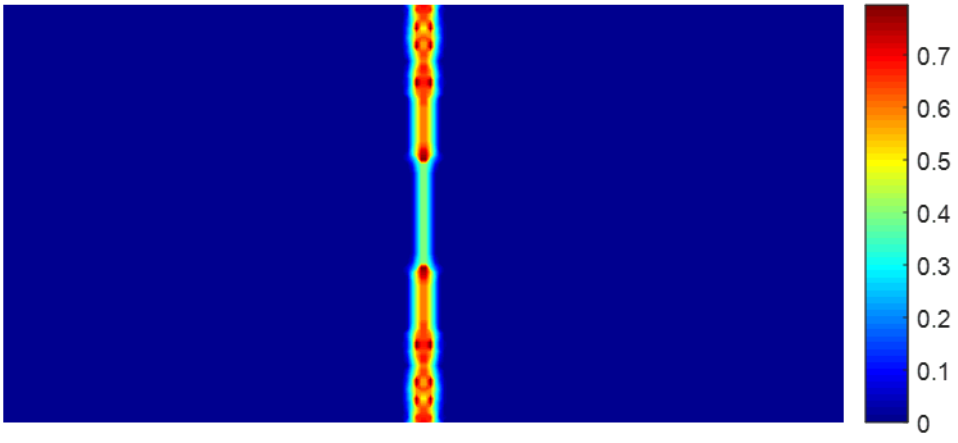

(c)

Figure 5.5 ANSYS results for the damage the plot of cracked lamina plate with fibre orientation of (a) $\theta = 0°$, (b) $\theta = 45°$ and (c) $\theta = 90°$

6. FREE VIBRATION AND BUCKLING OF CRACKED PLATE

In this chapter, the simulation of free vibration and buckling of the cracked plate is performed by the peridynamic model using ANSYS. The plates is modelled based on Chapter 3.5. A BEAM4 element in ANSYS represents every bond between material points, and the MASS21 element represents the mass of each material point. The various crack conditions are considered and compared the effect of crack length, crack direction and plate thickness. The peridynamic results are compared with experimental and numerical results from the referenced papers such as Krawczuk [2], Seifi and Khoda-Yari [20], Barton [21] and Qian et al. [22] In several cases, the verifications are done by comparing intact plate peridynamic results with results of FEM.

6.1 Buckling of Cracked Plate

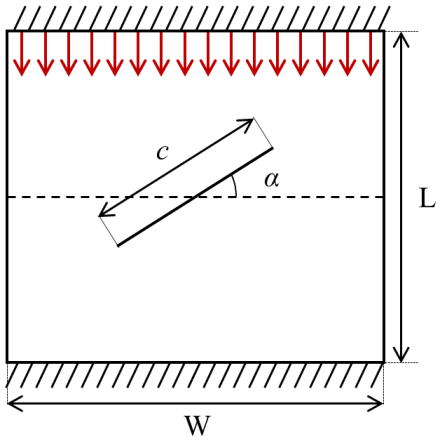

Figure 6.1 The geometry of a clamped-clamped plate with a crack

The plate illustrated in Figure 6.1 is subjected to a clamped-clamped condition (CFCF) with thickness h, crack length c and crack angle α. As mentioned above, the various states are considered, such as thickness from 8 to 12 mm, crack angle as 0°, 30° and 60°, and crack length ratio (c/W) as 0.1, 0.3 and 0.5. The plate shown in Figure 6.2 has the same conditions as in Figure 6.1. The difference is that the crack is located at the side of the plate.

The critical buckling loads of cracked plates are compared with results of Seifi et al. [20]. The plate dimensions are 240×240×12 mm^3, and the two opposite sides of the plate are

clamped, and the other sides are free, as shown in Figure 6.1. The Young's modulus is 70 MPa and Poisson's ratio is 0.33. The compressive load is acting on one side of the clamped edge. As explained in chapter 3.3, the peridynamic model has fictitious layers on both clamped sides of the plate. Compressive load is acting on material points within the real body as shown in Figure 6.3.

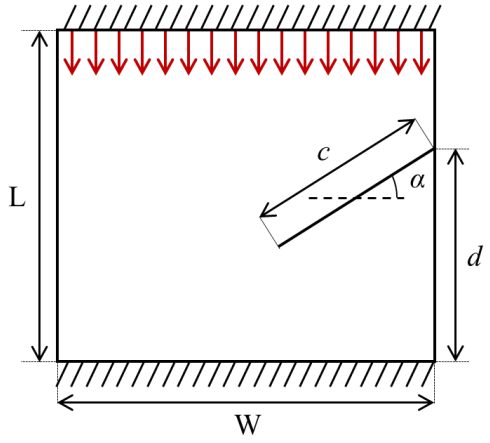

Figure 6.2 The geometry of a clamped-clamped plate with a side-crack

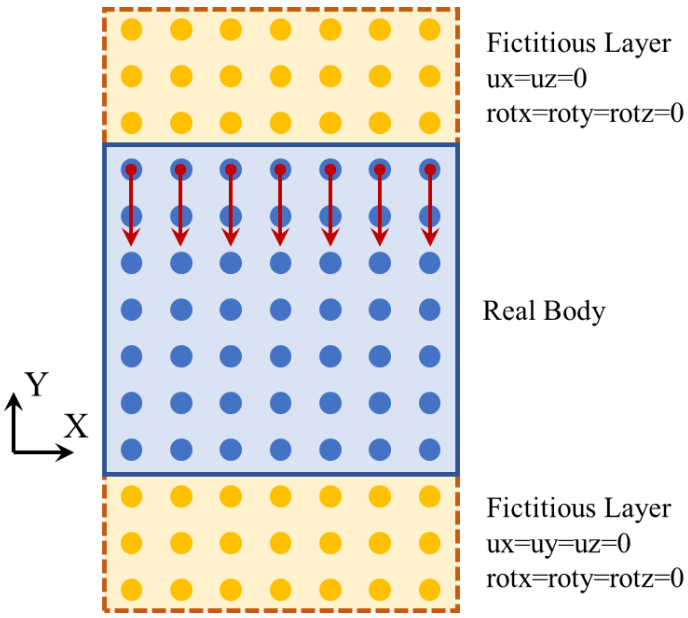

Figure 6.3 The boundary conditions of CFCF plate based on peridynamics

6.1.1 Results of the cracked plate with various parameters

The comparison of results is collected in Table 6.1. As shown in this the table, the critical buckling load increases with the initial crack angle. On the other hand, as the crack length increases the critical load decreases. Moreover, the longer crack length, the higher the effect of the crack angle. The errors between experimental and peridynamic values are within 8%, which means that the other results obtained by peridynamics can be considered as reliable.

The effect of plate thickness is also investigated. Before analysing the cracked plate, the results of the plate without a crack using peridynamics and FEM are compared to verify whether the peridynamic results are reliable or not in various thickness conditions. The FEM results are obtained by using shell element in ANSYS, and these results are summarized in Table 6.2. The differences between the two approaches are small and negligible, that is within 3%. So, it can be said that the peridynamic results of the plate with a crack can be considered reliable. When a plate is under compression, the plate produces internal energy. However, the part where the crack is present releases that energy. Therefore, it makes the plate easier to buckle. When a crack exists perpendicular to the load, this energy is released more quickly. It means that when the angle of the crack is zero degrees, and the length is long, it is easily buckled even for smaller forces.

Table 6.1 Comparison of experimental results for the critical buckling load of the cracked plate

Crack length ratio (c/w)	Crack angle (α)	Ref. [20] Experimental [N]	Peridynamics [N]	% Diff
0.1	0°	1627	1746.4	7.34
	30°	1651	1762.1	6.73
	60°	1674	1777.1	6.16
0.3	0°	1531	1562.6	2.06
	30°	1551	1631.7	5.20
	60°	1660	1729.4	4.18
0.5	0°	1317	1311.7	0.40
	30°	1396	1471.6	5.42
	60°	1636	1683.5	2.90

Table 6.2 Validation of peridynamic critical buckling load of the intact plate using FEM

Thickness [mm]	FEM buckling load [N]	Peridynamic buckling load [N]	% Diff
8	533.14	547.55	2.70
10	1033.2	1053.0	1.92
12	1768.9	1792.0	1.31

The results of a cracked plate are summarised in Table 6.3, and these results values are presented in graphs in Figure 6.4 and Figure 6.5. To see, the effect of each parameter, the non-dimensional critical buckling load (NCBL) k_M is used.

$$k_M = \frac{N_x W^2}{\pi^2 D} \quad with\, D = \frac{E h^3}{12(1-\nu^2)} \tag{6.1}$$

where D is flexural rigidity of plate which is the resistance caused by a structure in bending. In Table 6.3, it can be seen that the increase of thickness and initial crack angle cause an increase in critical buckling load.

According to Figure 6.4 and Figure 6.5, the NCBL decreases as the thickness increases. It is evident if the thickness increases at the same length and width of the plate, it means an increase of stiffness of the plate. NCBL is calculated as critical buckling load divided by stiffness. Thus as thickness increases, stiffness increases and, higher critical buckling load and lower NCBL should be expected.

Furthermore, regardless of the length of the crack, it can be seen that the thickness has similar effect on NCBL. This can be seen from the similar gradient of all NCBL-thickness graph. In addition, while the initial crack angle increases from 0° to 90°, the influence of crack length on NCBL decline. When the plates have same thickness, as the angle increases, the difference in value of NCBL depending on the crack length is reduced gradually.

When a plate is under compression, the plate produces internal energy but the part where the crack is a present release that energy. It makes the plate easier to buckle. If a section of a crack is perpendicular to the direction of compression force, the internal energy is released more easily. It means that when the angle of the crack is zero degrees, and the length of the crack is long, it is easily bent even for smaller forces.

Table 6.3 Peridynamic results for critical buckling load of a cracked plate

Thickness [mm]	Crack length ratio (c/W)	Crack angle (α)	Peridynamics [N]
8	0.1	0°	536.33
		30°	539.04
		60°	543.37
		90°	545.86
	0.5	0°	404.17
		30°	454.09
		60°	517.29
		90°	536.97
10	0.1	0°	1028.3
		30°	1036.0
		60°	1044.6
		90°	1049.7
	0.5	0°	772.81
		30°	868.77
		60°	991.91
		90°	1032.1
12	0.1	0°	1746.4
		30°	1762.1
		60°	1777.1
		90°	1786.4
	0.5	0°	1311.7
		30°	1471.6
		60°	1683.5
		90°	1755.7

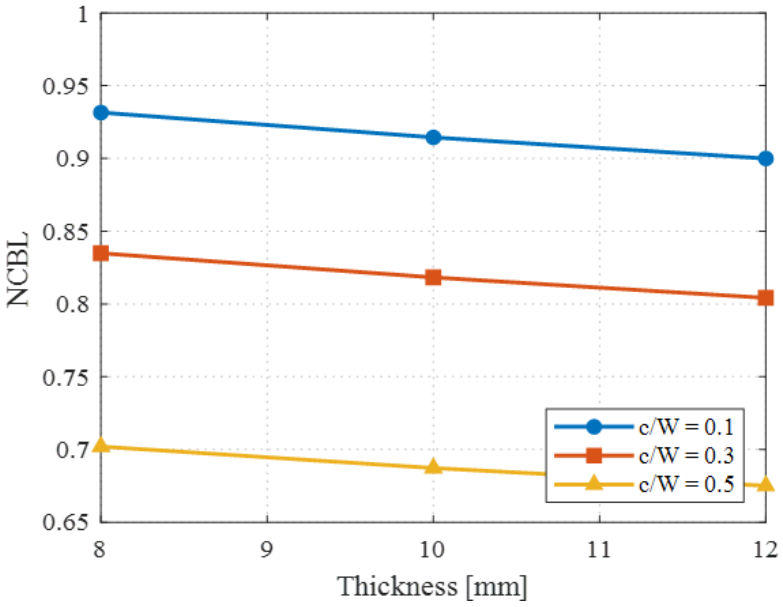

(a)

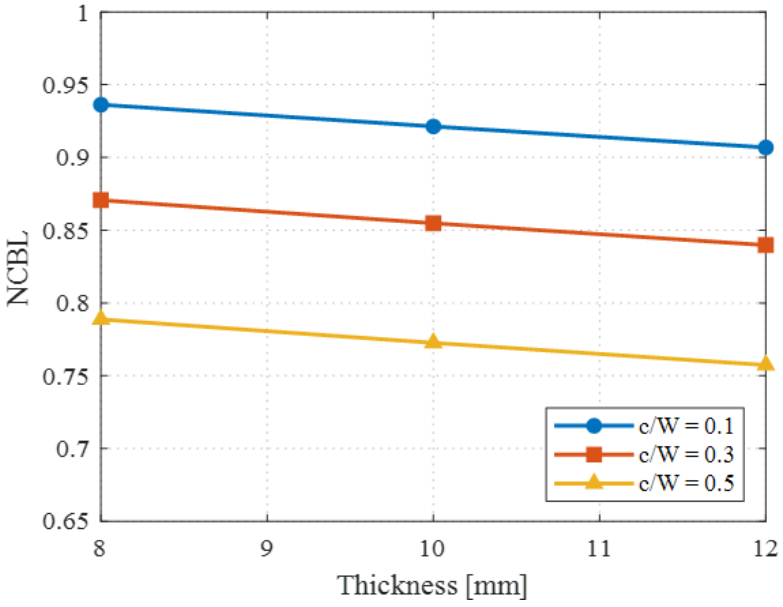

(b)

Figure 6.4 Effect of thickness on the non-dimensional critical buckling load ((a) $\alpha = 0°$, (b) $\alpha = 30°$)

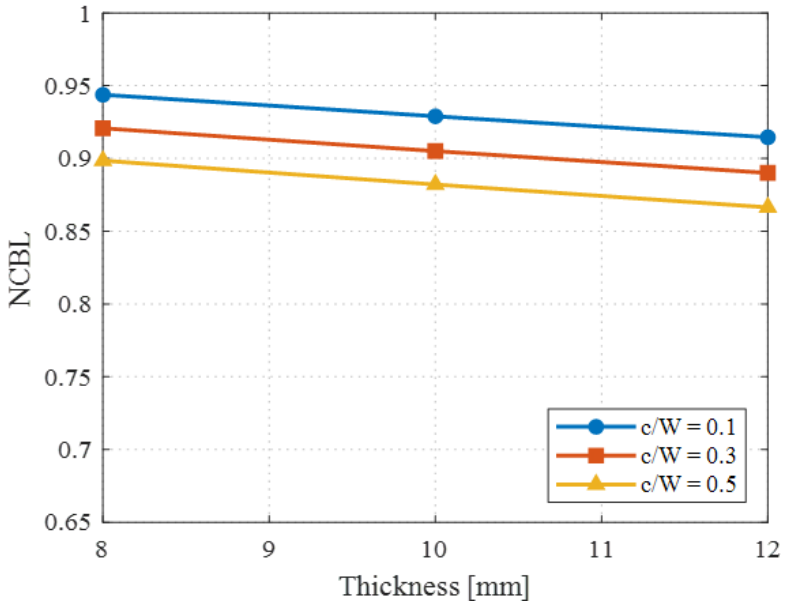

(a)

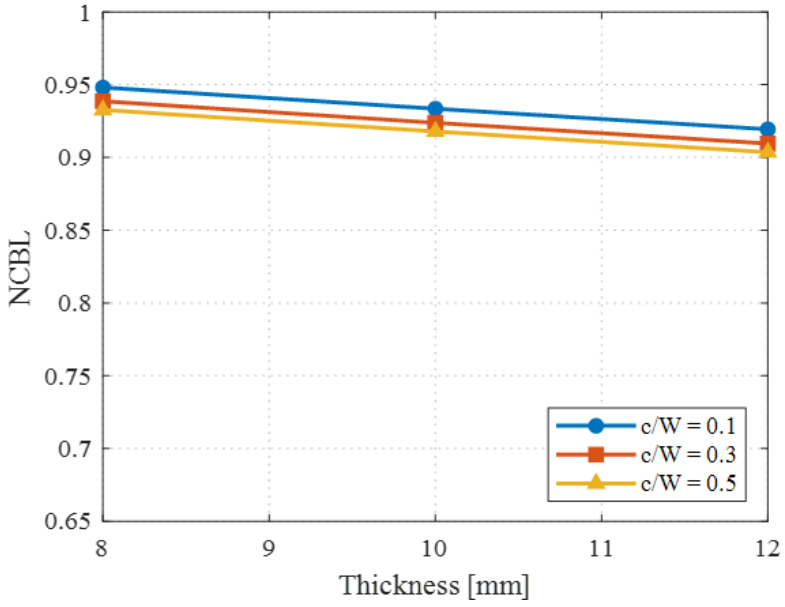

(b)

Figure 6.5 Effect of thickness on the non-dimensional critical buckling load ((a) $\alpha = 60°$, (b) $\alpha = 90°$)

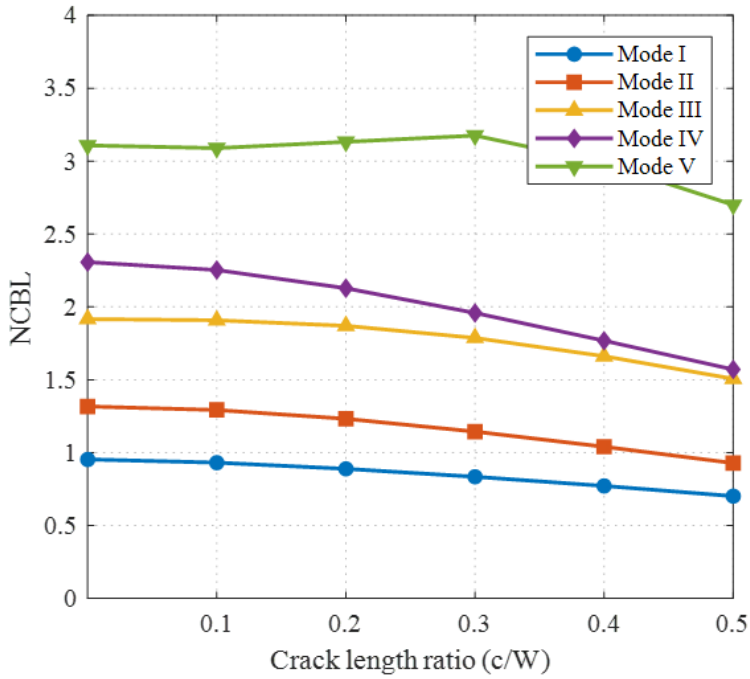

(a)

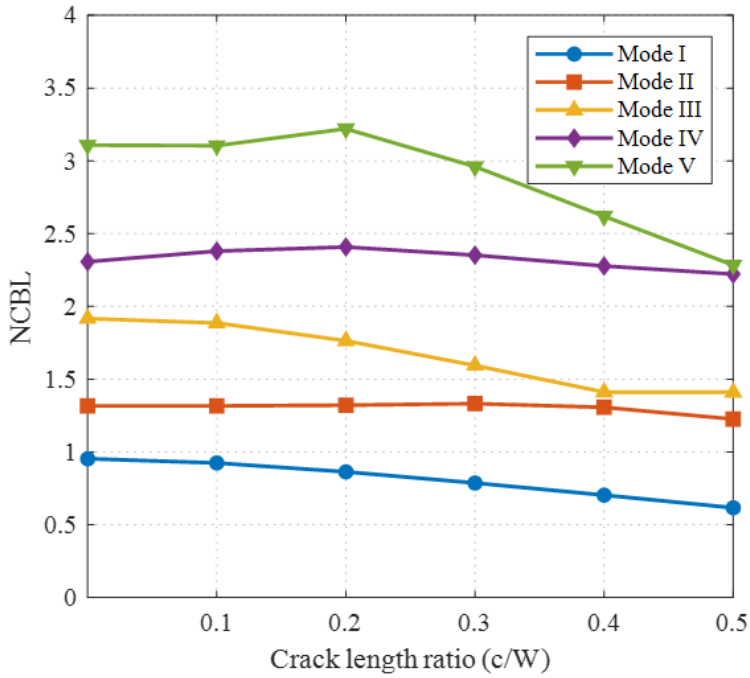

Figure 6.6 Variation of NCBL by crack length ((a) central crack, (b) side-edge crack)

Table 6.4 Peridynamic results for critical buckling load of side-edge cracked plate

Thickness [mm]	Crack angle (α)	Crack length ratio (c/W)	Crack location ratio (d/L)	Peridynamics [N]
8	0°	0.1	0.5	532.26
			0.7	542.96
			0.9	537.28
		0.5	0.5	355.16
			0.7	378.17
			0.9	398.41
	60°	0.1	0.5	543.28
			0.7	545.59
			0.9	546.56
		0.5	0.5	487.68
			0.7	486.02
			0.9	470.39
12	0°	0.1	0.5	1733.99
			0.7	1768.68
			0.9	1750.75
		0.5	0.5	1154.36
			0.7	1223.19
			0.9	1291.62
	60°	0.1	0.5	1771.34
			0.7	1778.73
			0.9	1781.68
		0.5	0.5	1587.05
			0.7	1580.10
			0.9	1533.00

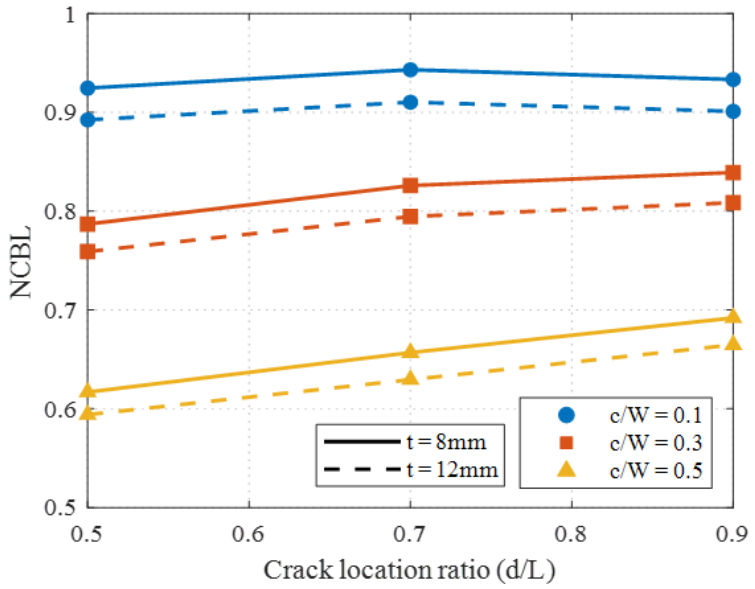

Figure 6.7 Effect of crack location on non-dimensional critical buckling load of side cracked plate

In Figure 6.6, the NCBL changes for each buckling mode according to the crack length for the central and side-edge cracked plate. The thickness of each plate is equal to 8mm and the material properties are the same as the plate considered earlier. The critical buckling load decreases as the length of the crack increases. It is evident that the NCBL is gradually reduced in the central crack case, and the side-edge crack results are slightly different from the central crack results.

The critical buckling loads of side cracked plate with different thickness, crack location, angle and size are summarized in Table 6.4. When the crack angle is zero degrees, the more the crack was placed in the middle of the plate ($d/L = 0.5$), the smaller the buckling load was required. In addition, when the crack is significantly large ($c/W = 0.5$), the critical buckling load gradually increases as the location of the crack moves away from the centre of the plate. When the size of the crack was small ($c/W = 0.1$), there was little change in buckling load with respect to its position.

As shown in Figure 6.7, the effect of the crack position on the NCBL compared. The length and position of the crack were changed in a plate having 8mm and 12mm thickness. As shown in the graph, NCBL increased as the crack is getting closer to the edge of the plate. Moreover, the slope shows that the shorter the length of the crack, the less the impact of the position. There is no significant difference between the two different thickness plates.

6.1.2 Results of the cracked plate with variable thickness

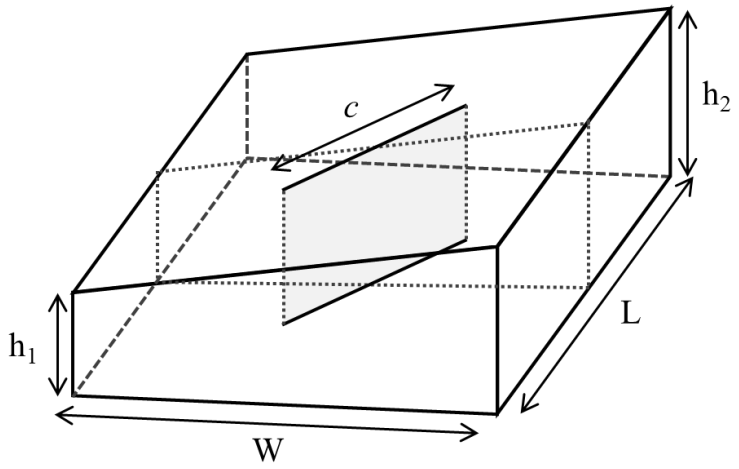

Figure 6.8 The geometry of a plate with a variable thickness along the length of the plate

In this section, the buckling analysis was performed for a plate with linearly increased thickness. The size of the plate is 240×240mm^2. As shown in Figure 6.8, the plate has a different thickness in the direction of width. The h_1 and h_2 are the minimum and maximum thickness of the plate, respectively. The plate is studied with different thickness ratio (h_2/h_1) changing from 1.1 to 2.0. Other crack-related constants, such as crack length and angle, are considered the same as the previous section. The material properties are also the same as the previous section, which is Young's modulus is 70 MPa and Poisson's ratio is 0.33.

Table 6.5 Comparison of FEM and peridynamic critical buckling load of the plate with variable thickness

Thickness ratio (h2/h1)	FEM buckling load [N]	Peridynamic buckling load [N]	% Diff
1.1	260.41	271.48	4.25
1.2	294.85	306.66	4.01
1.5	404.02	417.68	3.38
1.75	506.00	520.90	2.94
2.0	621.06	636.95	2.56

Firstly, the peridynamic model results of the plate was compared with the FEM results for verification purposes. The shell element of ANSYS was used for FEM results. The results are summarized in Table 6.5. It can be seen that the differences between peridynamics and FEM results are smaller than 5%. The critical buckling load increases as the thickness ratio is increases. This is because the more substantial the thickness ratio, the thicker the plate is, making the plate stronger. It means that greater load is needed, which increases the buckling load.

The critical buckling loads of cracked plate are recorded in Table 6.6. Similar to the intact plate case, the load increased as the ratio of thickness increased. The higher the thickness ratio, the more significant decrease in buckling load as the size of the crack increases. The change in crack angle with the same thickness ratio and length of the crack was not significant compared to other factors.

According to Figure 6.9 and Figure 6.10, the values of NCBL show that the crack affects the stiffness of the plate. The thickness ratio has a significant effect, as with other factors, in buckling analysis. The value of NCBL decreases as the ratio of thickness increases. As with the previous results, the smaller angle of crack, the more significant impact of the length of the crack. The gradient of all graphs is similar, indicating that the influence of the ratio of thickness is constant regardless of the crack length and angle.

Table 6.6 Peridynamic results for critical buckling load of the cracked plate with variable thickness

Crack angle (α)	Crack length ratio (c/W)	Thickness ratio (h_2/h_1)	Peridynamics [N]
0°	0.1	1.1	265.45
		1.2	299.82
		1.5	408.32
		2.0	622.63
	0.5	1.1	200.11
		1.2	224.61
		1.5	300.01
		2.0	448.36
30°	0.1	1.1	267.39
		1.2	302.05
		1.5	411.47
		2.0	627.54
	0.5	1.1	226.80
		1.2	254.36
		1.5	339.33
		2.0	506.74
60°	0.1	1.1	269.62
		1.2	304.60
		1.5	415.05
		2.0	633.03
	0.5	1.1	256.84
		1.2	288.73
		1.5	387.41
		2.0	579.96

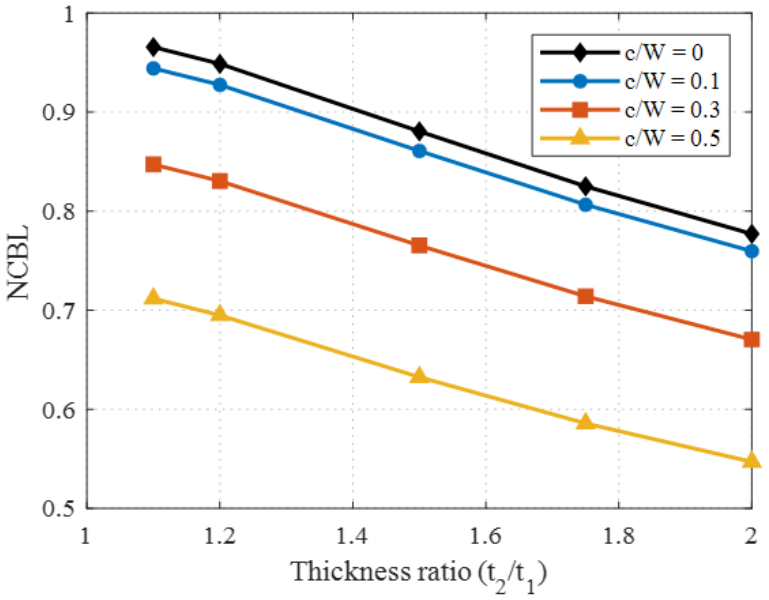

(a)

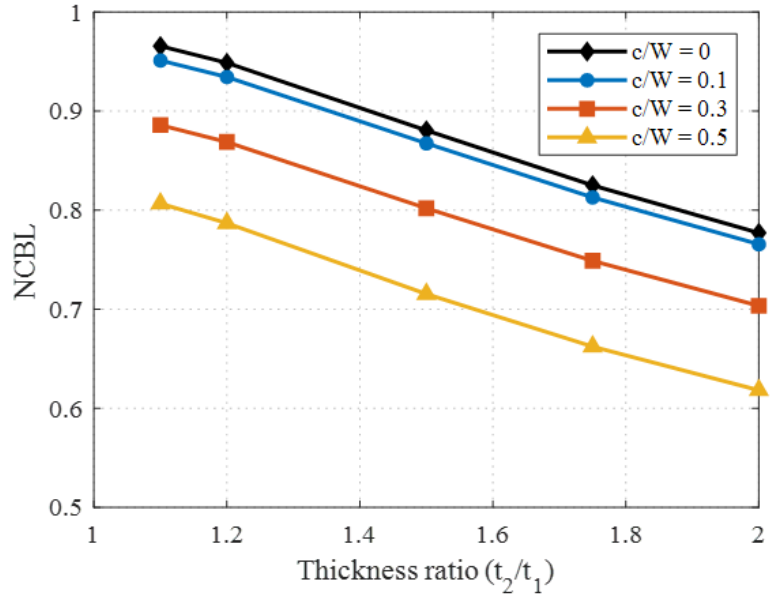

(b)

Figure 6.9 Effect of thickness ratio on the non-dimensional critical buckling load ((a) α=0°, (b) α=30°)

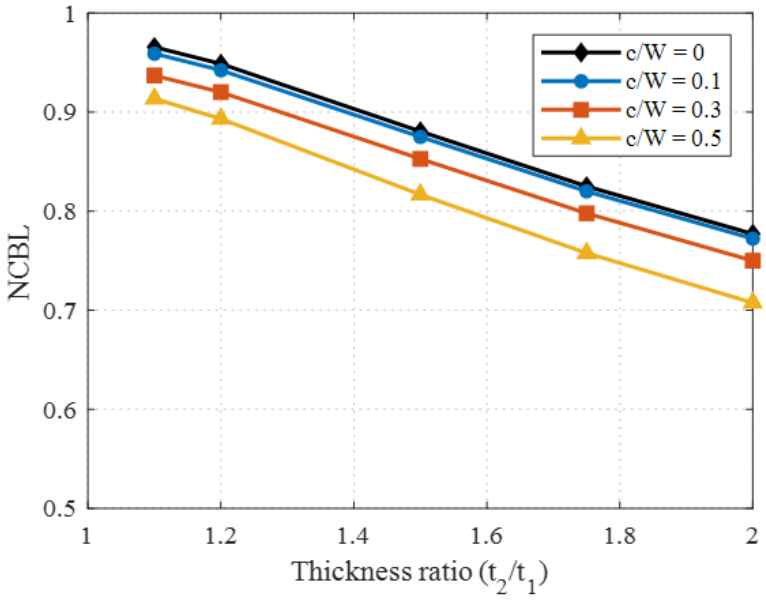

(a)

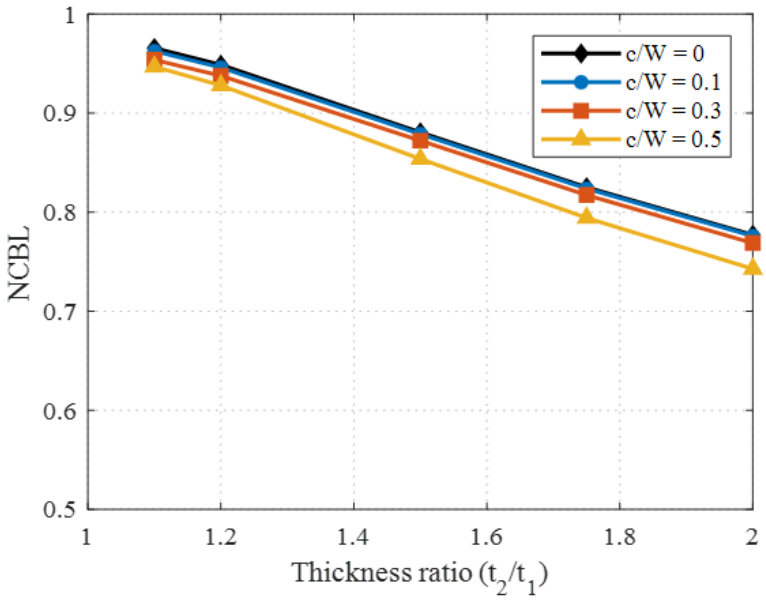

(b)

Figure 6.10 Effect of thickness ratio on the non-dimensional critical buckling load ((a) α=60°, (b) α=90°)

6.2 Free Vibration of Cracked Plate

In this section, the free vibration simulation is performed to obtain the natural frequencies of the plate. At first, the validation procedure is performed by comparing with the results of other papers.

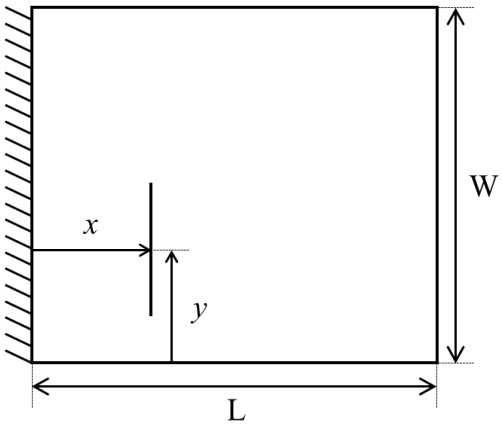

Figure 6.11 The geometry of a cantilever plate with a crack

6.2.1 Results of the cracked plate with various parameter

The natural frequency of the cantilever plate with dimensions of 240×240mm^2 and thickness of 2.75mm are summarized in Table 6.7 and Table 6.8. The plate is made of aluminium with Young's modulus of 67 GPa, Poisson's ratio of 1/3 and mass density of 2800kg/m^3. The Table 6.7 contains the natural frequencies of the plate without crack. The peridynamic results are compared with numerical, theoretical results of Krawczuk, M. [2], Barton, M. [21], respectively, and the finite element results using ANSYS shell element. In all four cases, the natural frequencies are similar to each other and the differences between FE and peridynamic results are smaller than 3%.

In Table 6.8, the ratios of natural frequencies of cracked plated to intact plate are compared with values from referenced papers. The crack is parallel with fixed edge and length is 34 mm, and centre of cracked is located 90 mm apart from the lower right corner of the plate ($x = y = 90$ mm). This model is illustrated in Figure 6.11. The good agreement between peridynamic results and the others are obtained. Therefore, it can be said that the peridynamic natural frequencies are reliable in other similar cases as well.

Moreover, an analysis to investigate the effect of crack length, crack angle and plate thickness is performed. The material properties are the same as Table 6.7. The plate is subjected to a clamped-clamped condition, like Figure 6.1, and the results are shown in Table 6.9. Likewise, in the simulation of free vibration, we used the non-dimensional value of frequency.

$$\Omega = \omega W^2 \sqrt{\frac{\rho}{Eh^3}} \tag{6.2}$$

In Table 6.9 and Figure 6.12, similar information is obtained with Figure 6.4, Figure 6.5 and Table 6.3. Similar to buckling results, the thicker plate has higher rigidity, which causes higher natural frequencies and lower non-dimensional frequencies. It also shows that the increase of crack angle and decrease of crack length caused an increase in natural frequency. Additionally, as shown in Figure 6.13, the line of $c/L = 0.1$ have similar non-dimensional frequency regardless of a crack angle. It means that the shorter crack length, the lower impact of crack angle. As the crack angle increases, the interval of each graph line decreases. This means that the larger the angle of the crack, the smaller the influence of the crack length.

Table 6.7 Validation of peridynamic result with other methods of intact plate

Mode	Ref. [2] [Hz]	Ref. [21] [Hz]	FEM [Hz]	Peridynamics [Hz]	% Diff
1	41.49	40.39	39.36	40.452	2.70
2	99.87	96.94	94.89	101.10	1.92
3	255.91	242.36	239.92	249.77	1.31

Table 6.8 The ratio of natural frequencies of cracked plate to intact plate

Mode	Ref. [2] numerical	Ref. [22] theoretical	Ref. [22] experimental	Peridynamics
1	0.9891	0.9931	0.9917	0.9909
2	0.9985	0.9989	0.9981	0.9978
3	0.9826	0.9837	0.9807	0.9899

The Figure 6.14, Figure 6.15 and Figure 6.16 show the first five-mode shapes for three cases of crack angle (0°, 30° and 60°). Each figure represents the central cracked plate, the central cracked plate with variable thickness and side-edge crack plate, respectively. All plates are under clamped-clamped condition (CFCF) and have the same material properties. In Figure 6.14, it can be seen that each mode changes as the crack angle increases. In particular, there are significant differences in modes of third or higher. The Figure 6.15 shows the mode shape for the plate with linearly varying thickness as described in Figure 6.8. The thickness ratio is 2, and the right side of the plate is the thick side. Overall, it can be seen that the centre of each vibration mode shape is tilted to the left, which is the thin side of the plate. Other than this, it has a very similar mode shape to Figure 6.14.

Table 6.9 Peridynamic results for natural frequencies of the cracked plate (CFCF)

Thickness [mm]	Crack length ratio (c/W)	Crack angle (α)	Peridynamics [Hz]
8	0.1	0°	706.18
		30°	707.99
		60°	709.99
	0.3	0°	676.32
		30°	686.03
		60°	703.15
	0.5	0°	631.05
		30°	657.55
		60°	695.31
10	0.1	0°	874.09
		30°	874.30
		60°	879.50
	0.3	0°	837.09
		30°	848.17
		60°	870.63
	0.5	0°	780.83
		30°	812.47
		60°	860.72
12	0.1	0°	1040.0
		30°	1038.9
		60°	1045.87
	0.3	0°	994.86
		30°	1007.3
		60°	1035.1
	0.5	0°	927.95
		30°	964.54
		60°	1022.98

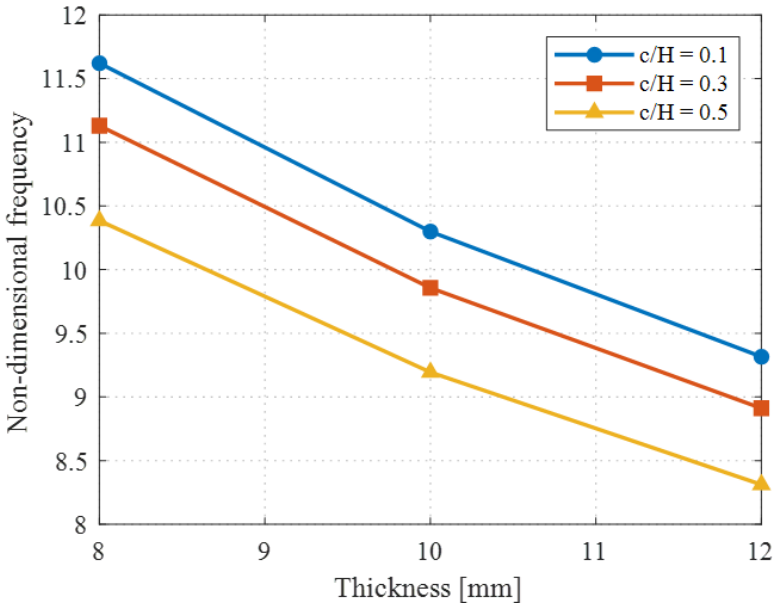

(a)

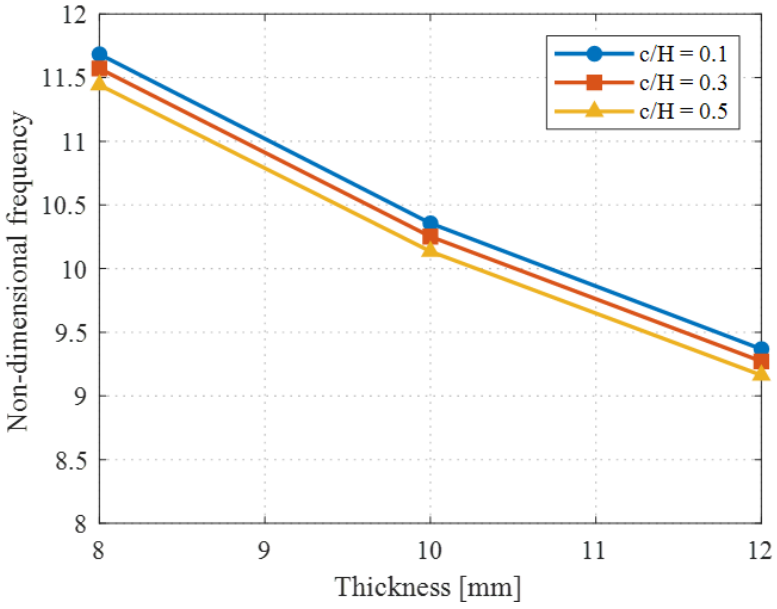

(b)

Figure 6.12 Effect of thickness on non-dimensional frequency

((a) $\alpha = 0°$, (b) $\alpha = 60°$)

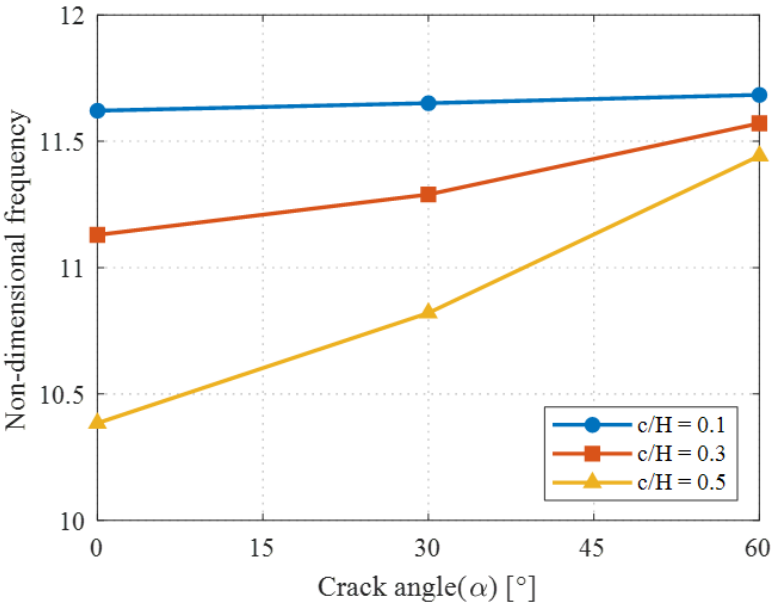

(a)

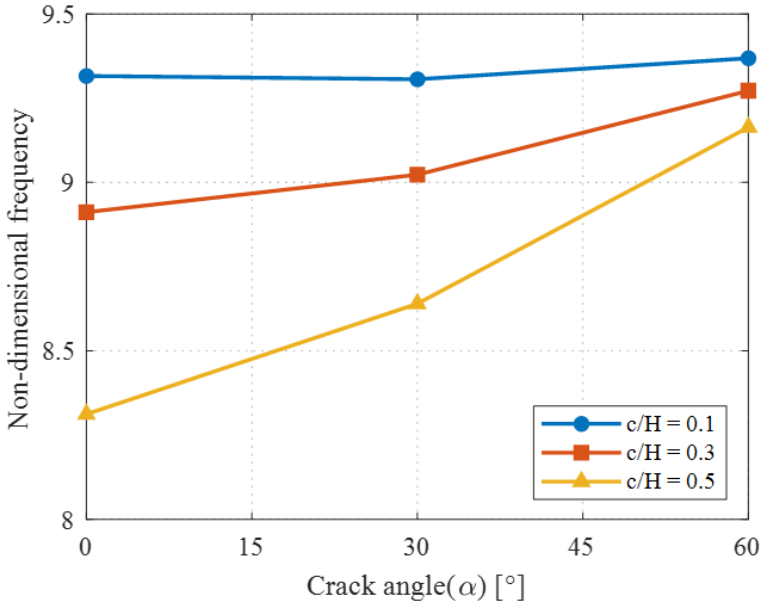

(b)

Figure 6.13 Effect of crack angle on non-dimensional frequency

((a) $h = 8$ mm, (b) $h = 12$ mm)

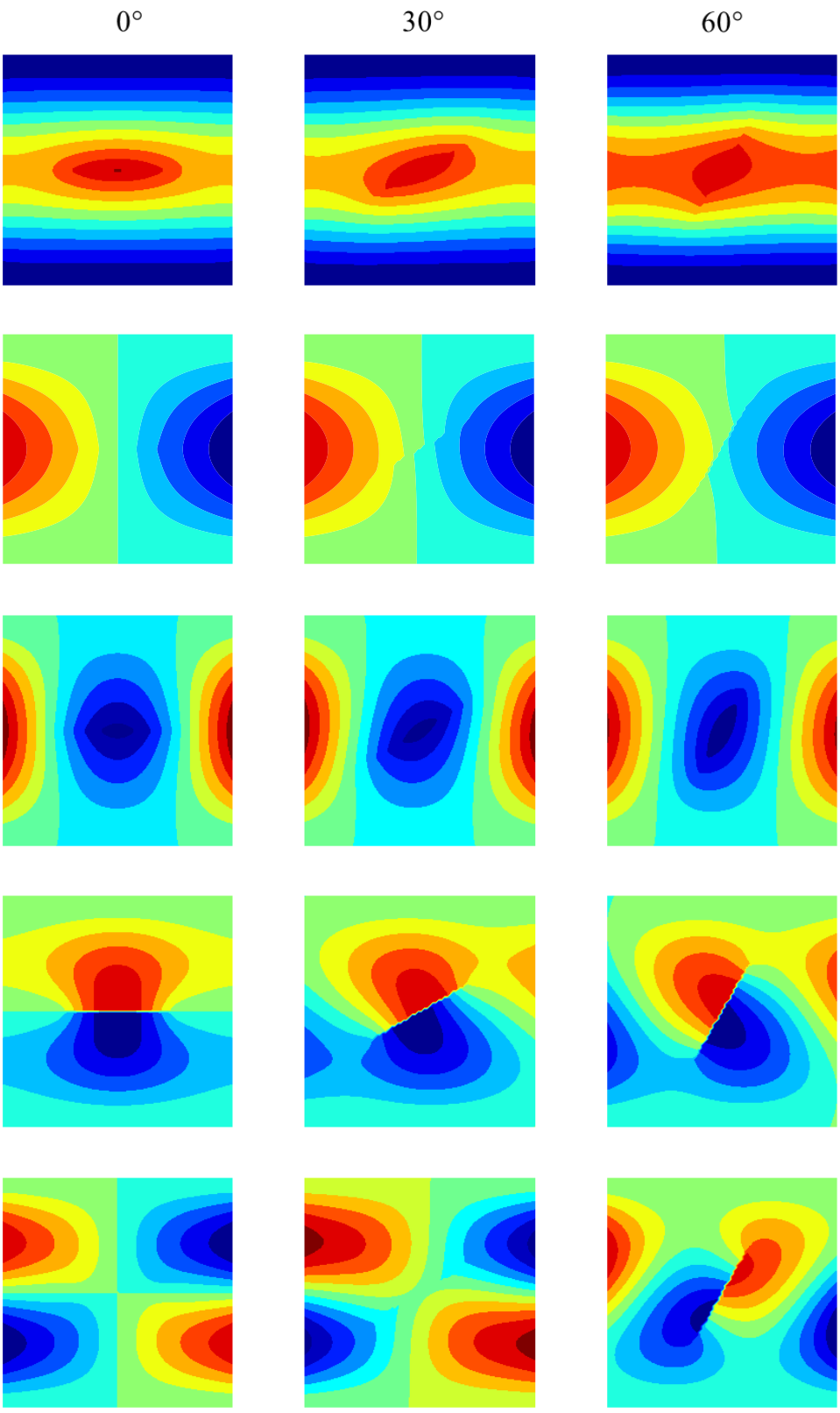

Figure 6.14 First five vibration mode shape of central cracked plate (CFCF)

(Mode: from top to bottom; 1st, 2nd, 3rd, 4th and 5th)

(Crack angle: from left to right; 0°, 30° and 60°)

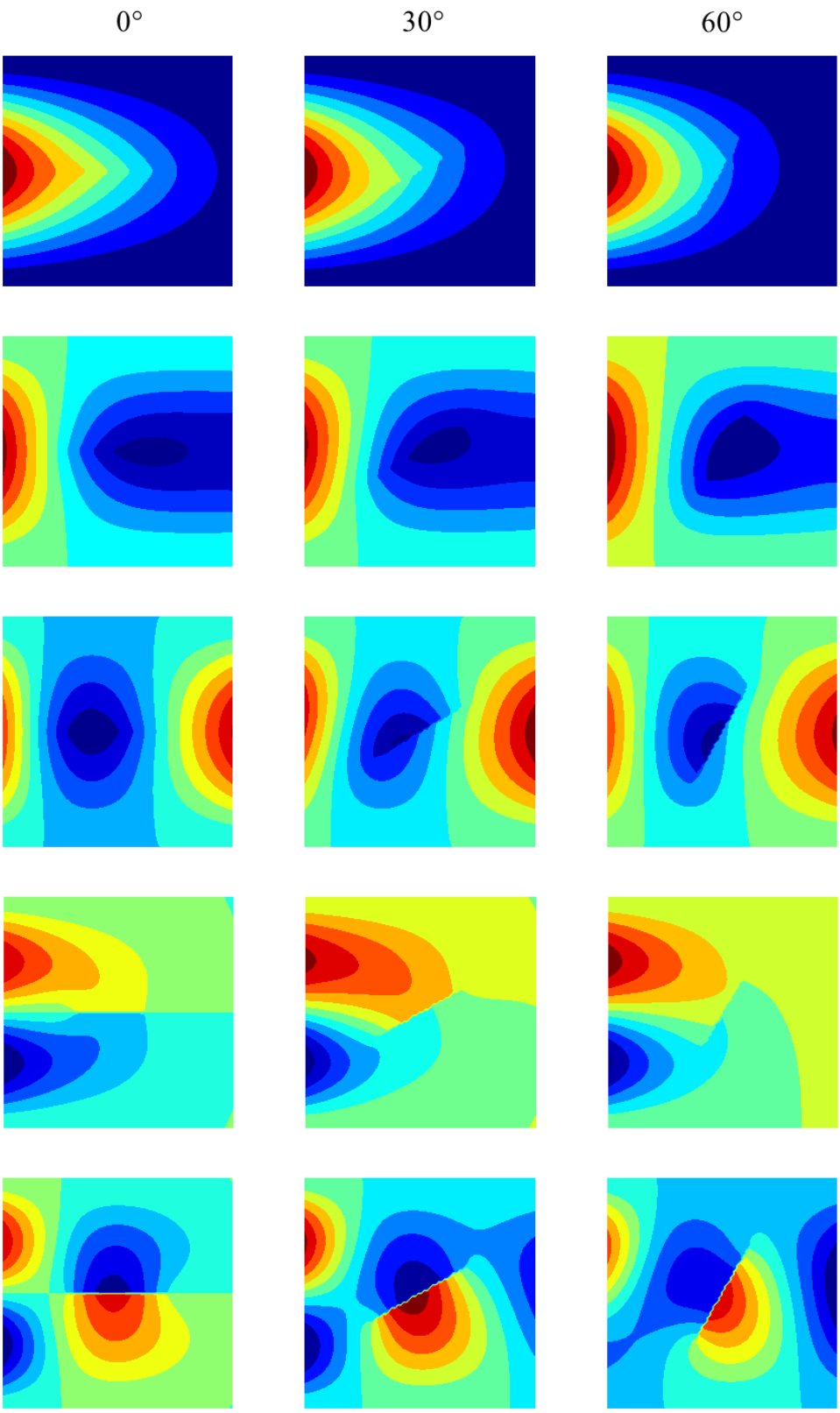

Figure 6.15 First five vibration mode shape of a variable thickness cracked plate (CFCF)

(Mode: from top to bottom; 1st, 2nd, 3rd, 4th and 5th)

(Crack angle: from left to right; 0°, 30° and 60°)

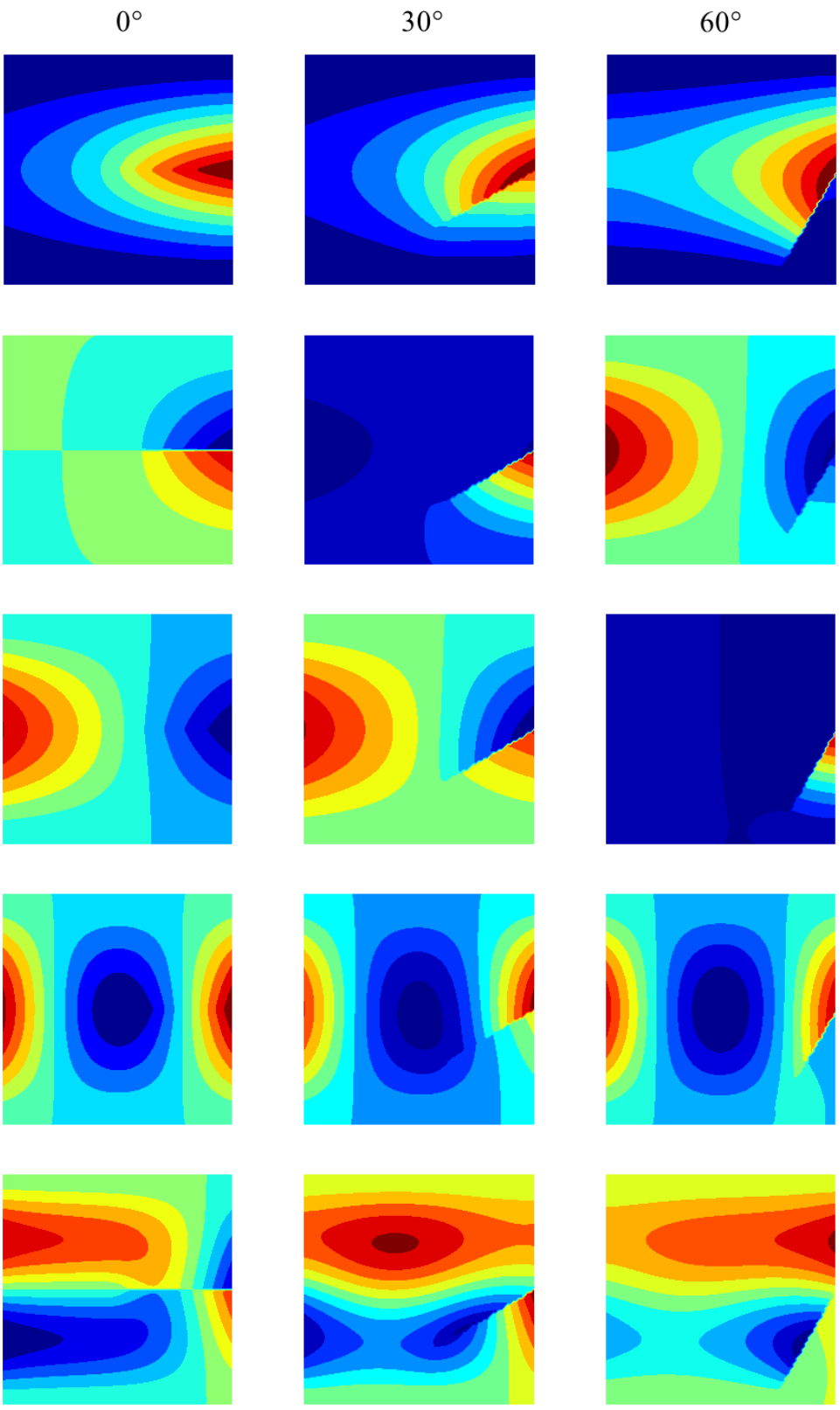

Figure 6.16 First five vibration mode shape of the side-edge cracked plate (CFCF)

(Mode: from top to bottom; 1st, 2nd, 3rd, 4th and 5th)

(Crack angle: from left to right; 0°, 30° and 60°)

7. CONCLUSION

In this thesis, a research about peridynamics, which has the advantage of being able to analysis the cracked structures, is performed. The peridynamic theory was implemented to a commercial finite element analysis tool, and various structural analyses that may be required in the offshore platforms and ship structures are carried out. In particular, the changes in the characteristics of the cracked structure, which are the most common problems, are discussed. The investigation about changes of critical buckling loads and natural frequencies according to the location, size, and angle of the crack is conducted and how each factor affects the characteristic value of the structure is determined. In addition, various analyses were attempted using finite element analysis software based on peridynamics such as crack propagation of fibre reinforced material.

- It can be seen that the crack propagation of the fibre reinforced material has different crack propagation results depending on the fibre direction of the plate, as described in chapter 0. Very similar results can be obtained both using MATLAB and ANSYS, i.e. the language-based program and finite element software, respectively.

- In chapter 6, a case study was conducted on changes in cracked structures due to factors such as the location, inclination and size of cracks. First, the peridynamic model results are compared with experimental results of other papers to prove the validity of it, and it gave good results with a margin of error of 8%. Besides, the critical buckling load and natural frequencies of the non-cracked plates are investigated and compared with the finite element analysis results. It also showed that accuracy that has an error of less than 5%, and it can be said that the reliability of peridynamic model is validated.

- Changes in the length, angle and position of crack and thickness and thickness change ratio of the plate were considered as research parameters, and the effects of each element on the critical buckling load and natural frequency of the plate were analysed. The thicker the plate, the greater buckling load was required, the longer the length of the crack and the more perpendicular the crack was to the direction of the force, the easier it was to be buckled even in smaller forces. Natural frequency also had a higher value as the stiffness of the plate increases, and it can be seen that the position and angle of the crack affect mode shape of the plate.

REFERENCES

[1] S. A. Silling and E. Askari, "A meshfree method based on the peridynamic model of solid mechanics," in *Computers and Structures,* 2005.

[2] M. Krawczuk, "Natural vibrations of rectangular plates with a through crack," Springer-Verlag, 1993.

[3] M. R. Khedmati, P. Edalat and M. Javidruzi, "Sensitivity analysis of the elastic buckling of cracked plate elements under axial compression," *Thin-Walled Structures,* vol. 47, no. 5, pp. 522-536, 2009.

[4] K. Markstrom and B. Storakers, "Buckling of cracked members under tension," *International Journal of Solids and Structures,* vol. 16, pp. 217-229, 1980.

[5] D. Shaw and Y. Huang, "Buckling behavior of a central cracked thin plate under tension," *Engineering Fracture Mechanics,* vol. 35, no. 6, pp. 1019-1027, 1990.

[6] M. Nerantzaki and J. Katsikadelis, "Buckling of plates with variable thickness an analog equation solution," *Engineering Analysis with Boundary Elements,* vol. 18, no. 2, pp. 149-154, 1996.

[7] P. P. Minh, T. Van Do, D. H. Duc and N. D. Duc, "The stability of cracked rectangular plate with variable thickness using phase field method," *Thin-Walled Structures,* vol. 129, pp. 157-165, 2018.

[8] D. H. Doan, T. Van Do, P. M. Pham and N. D. Duc, "Validation simulation for free vibration and buckling of cracked Mindlin plates using phase-field method," *Mechanics of Advanced Materials and Structures,* pp. 1-10, 2018.

[9] H. C. Zeng, C. S. Huang, A. W. Leissa and M. J. Chang, "Vibrations and stability of a loaded side-cracked rectangular plate via the MLS-Ritz method," *Thin-Walled Structures,* vol. 106, pp. 459-470, 2016.

[10] Y. V. Kumar and J. K. Paik, "Buckling analysis of cracked plates using hierarchical trigonometric functions," *Thin-Walled Structures,* vol. 42, no. 5, pp. 687-700, 2004.

[11] R. W. Macek and S. A. Silling, “Peridynamics via finite element analysis,” *Finite Elements in Analysis and Design,* vol. 43, no. 15, pp. 1169-1178, 2007.

[12] “EMU website,” [Online]. Available: https://www.emich.edu/.

[13] Z. Yang, E. Oterkus, C. T. Nguyen and S. Oterkus, “Implementation of peridynamic beam and plate formulations in finite element framework,” *Continuum Mechanics and Thermodynamics,* vol. 31, no. 1, pp. 301-315, 2019.

[14] E. Madenci, C. Diyaroglu and N. D. Phan, “ANSYS implementation of peridynamics for deformation of orthotropic materials,” 2018.

[15] E. Madenci and E. Oterkus, Peridynamic Theory and Its Applications, New York, NY: Springer New York, 2014.

[16] S. Silling, “Linearized theory of peridynamic states,” *Journal of Elasticity,* vol. 99, no. 1, pp. 85-111, 2010.

[17] C. Diyaroglu, E. Oterkus, S. Oterkus and E. Madenci, “Peridynamics for bending of beams and plates with transverse shear deformation,” *International Journal of Solids and Structures,* Vols. 69-70, pp. 152-168, 2015.

[18] N. Stephen, “Mindlin plate theory: best shear coefficient and higher spectra validity,” *Journal of Sound and Vibration,* vol. 202, no. 4, pp. 539-553, 1997.

[19] E. Oterkus and E. Madenci, “Peridynamic analysis of fiber-reinforced composite materials,” *Journal of Mechanics of Materials and Structures,* vol. 7, no. 1, pp. 45-84, 2012.

[20] R. Seifi and N. Khoda-Yari, “Experimental and numerical studies on buckling of cracked thin-plates under full and partial compression edge loading,” *Thin-Walled Structures,* vol. 49, no. 12, pp. 1504-1516, 2011.

[21] M. Barton, “Vibration of rectangular and skew cantilever plates,” *Journal of Applied Mechanics Transactions of the ASME,* vol. 18, p. 129–134, 1951.

[22] G.-L. Qian, S.-N. Gu and J.-S. Jiang, “A finite element model of cracked plates and application to vibration problems,” 1991.

[23] R. Seifi and A. R. Kabiri, “Lateral Load effects on buckling of cracked plates under tensile loading,” *Thin-Walled Structures,* vol. 72, pp. 37-47, 2013.

[24] E. Oterkus, I. Guven and E. Madenci, “Impact damage assessment by using peridynamic theory,” *Central European Journal of Engineering,* vol. 2, no. 4, pp. 523-531, 2012.

[25] A. Nasirmanesh and S. Mohammadi, “XFEM buckling analysis of cracked composite plates,” *Composite Structures,* vol. 131, pp. 333-343, 2015.

[26] Y. L. Hu and E. Madenci, “Bond-based peridynamic modeling of composite laminates with arbitrary fiber orientation and stacking sequence,” *Composite Structures,* vol. 153, pp. 139-175, 2016.

[27] J. Guo, W. Gao, Z. Liu, X. Yang and F. Li, “Study of dynamic brittle fracture of composite lamina using a bond-based peridynamic lattice model,” *Advances in Materials Science and Engineering,* pp. 1-16, 2019.

[28] C. Diyaroglu, “Peridynamics and its applications in marine structures — University of Strathclyde,” 2015.

[29] R. De Frias Lopez, “A 3D finite beam element for the modelling of composite wind turbine wings,” 2013.

[30] C. Cui, P. Yang, T. Xia and J. Du, “Assessment of residual ultimate strength of cracked steel plates under longitudinal compression,” *Ocean Engineering,* vol. 121, pp. 174-183, 2016.

[31] F. Baber, V. Ranatunga and I. Guven, “Peridynamic modeling of low-velocity impact damage in laminated composites reinforced with z-pins,” *Journal of Composite Materials,* vol. 52, no. 25, pp. 3491-3508, 2018.

[32] C. Diyaroglu, E. Oterkus, E. Madenci, T. Rabczuk and A. Siddiq, “Peridynamic modeling of composite laminates under explosive loading,” *Composite Structures,* vol. 144, pp. 14-23, 2016.